Check for updates

AGU100 ADVANCING EARTH AND SPACE SCIENCE

JGR

Journal of Geophysical Research: Atmospheres

RESEARCH ARTICLE
10.1029/2018JD028595

A Comparison of Cloud Classification Methodologies: Differences Between Cloud and Dynamical Regimes

A. J. McDonald[1,2] **and S. Parsons**[2]

[1]Gateway Antarctica, University of Canterbury, Christchurch, New Zealand, [2]School of Physical and Chemical Sciences, University of Canterbury, Christchurch, New Zealand

Key Points:
- Cloud and Dynamic regimes are derived via the Self-Organizing Map method from common data sets
- The Cloud regime is the better of the current classifications based on statistical analysis
- Independent ISCCP FD and CloudSat data also show the higher value of the Cloud regime in this case

Supporting Information:
- Supporting Information S1
- Figure S1
- Figure S2

Correspondence to:
A. J. McDonald,
adrian.mcdonald@canterbury.ac.nz

Citation:
McDonald, A. J., & Parsons, S. (2018) A comparison of cloud classification methodologies: Differences between cloud and dynamical regimes. *Journal of Geophysical Research: Atmospheres*, *123*, 11,173–11,193. https://doi.org/10.1029/2018JD028595

Received 1 MAR 2018
Accepted 6 JUL 2018
Accepted article online 14 JUL 2018
Published online 9 OCT 2018

Abstract Classifications of cloud data into Cloud Regimes (CRs) and compositing based on meteorological parameters, Dynamic Regimes (DRs), are often used in the analysis of clouds. We compare CR and DR classifications to understand the relative merits of these approaches and develop a comparison methodology for future studies. We apply the Self-Organizing Map technique to International Satellite Cloud Climatology Project (ISCCP) D1 joint histograms to produce a CR and ERA-Interim pressure vertical velocity output to produce a DR. The CR created improves the separation between high-level CRs compared to previous work. Composites of ISCCP joint histogram data using the DR produce coherent groupings similar to those in the CR scheme particularly in regions of ascent. Both classifications display coherent geographical patterns and reproduce relationships between vertical velocity and cloud properties. However, the CR produces more coherent clusters with higher intracluster similarity and a greater range of independent cloud classes. Independent tests of composites using ISCCP FD output show that the regional variability of longwave cloud radiative effect for particular nodes are significantly higher in the DR than the CR scheme suggesting a poorer classification. Composite mean CloudSat reflectivity-altitude joint histograms represent all major cloud types in the CR scheme, while the current DR grouping is less coherent and misses classes. This suggests that the CR scheme is a more useful classification than the DR scheme based solely on vertical velocity data. Contingency table analysis indicates a low association between these classifications, suggesting combining these schemes would be valuable.

Plain Language Summary The two most common methods for the statistical evaluation of cloud properties are the derivation of cloud regimes and compositing based on specific ranges of meteorological parameters, dynamic regimes. This study compares these methods using the machine learning techniques and independent data sets. The cloud regime method is shown to provide a more meaningful classification. However, classification methodologies that can incorporate both methods will have additional value.

1. Introduction

The two most common methods for the statistical evaluation of cloud properties are the derivation of cloud regimes (CRs) and compositing based on specific ranges of meteorological parameters, dynamic regimes (DRs). These methodologies allow a statistical evaluation of cloud properties which retains the general characteristics of specific cloud systems after averaging (Jakob, 2003).

The derivation of CRs is detailed in Jakob and Tselioudis (2003), Tselioudis et al. (2013), and McDonald et al. (2016), this methodology relies on clustering satellite cloud data, most commonly using the k-means clustering technique. Composite analysis of cloud properties based on specific ranges of dynamical parameters has also been used (Bony et al., 2004; Haynes et al., 2011; Li et al., 2014). In this study, we aim to evaluate and compare the CR and DR approaches applied to a range of data sets to examine the strengths and limitations of these methods. A secondary goal is to understand the relationship between the clusters produced using these two methodologies.

We now discuss various aspects of the schemes based on previous work. Williams and Brooks (2008) were among the first to show that CRs were useful in model evaluation because they provide a summary of model performance across a range of synoptic situations. They also identified that CRs tend to be broadly aligned with large-scale atmospheric processes. CRs are also sometimes referred to as weather states (WSs), for example, Tselioudis et al. (2013), however this terminology is not used in this study because of the possibility of

©2018. American Geophysical Union. All Rights Reserved.

confusion with dynamical regimes. The relationship between the CR radiative properties, geographic and seasonal occurrence derived from observations, and model output can be compared to identify sources of model errors (Williams & Webb, 2009). The differences between the model and observations in the CR framework can result from both incorrect occurrences of different regimes and errors in the cloud properties within those regimes. Thus, CR schemes are often helpful in identifying compensating errors (Schuddeboom et al., 2018). Studies have also demonstrated that the CRs are useful for decomposing and differentiating the radiative effects and contributions of prevailing clouds (Haynes et al., 2011; McDonald et al., 2016; Oreopoulos & Rossow, 2011; Oreopoulos et al., 2014, 2016; Tselioudis et al., 2013; Williams & Webb, 2009).

Passive observations have been the most popular choice for creating CRs because of their wide spatial and temporal coverage. One resultant weakness of the CR approach is the potential for misinterpretation of radiance observations in terms of cloud properties (Chen & Del Genio, 2009). In particular, instrumental factors mean that there is significant uncertainty in the amount of thin cirrus observed by International Satellite Cloud Climatology Project (ISCCP) according to Williams and Webb (2009). In situations where cloud types overlap vertically in multiple layers, CRs based on passive observations can also be misleading.

Mace and Wrenn (2013) examined the cloud-type definitions related to specific portions of the ISCCP cloud optical depth versus cloud top pressure joint histograms, originally detailed in Rossow and Schiffer (1999), using measurements from the CloudSat Cloud Profiling Radar and the Cloud-Aerosol Lidar and Infrared Pathfinder Satellite Observations lidar in the equatorial Pacific. They found that with the exception of the thin cirrus and stratocumulus types, none of the cloud types based on the ISCCP joint histogram are related to unique distributions of geometrically defined layer types, but instead are populated by diverse sets of hydrometeor layers whose bulk properties combine to produce the specific radiative signatures. This is counter to results in Y. Y. Zhang et al. (2007) which indicated a general correspondence between ISCCP and CloudSat CRs in the tropics.

Further work in Leinonen et al. (2016) highlighted the regional variability in each cluster of a CR derived from Moderate Resolution Imaging Spectroradiometer (MODIS) observations. The utility of their regimes is shown to depend on the regimes' ability to identify cloud structures associated with distinct meteorological conditions. To test their regimes, they derive composites of CloudSat data according to their CRs. Reflectivity-altitude joint histograms reveal different structures for each regime, but also differences within regimes as a function of region. They hypothesize that the region-dependent variability within clusters results from differences in meteorological environment. Regional radiative differences between ISCCP WSs were also highlighted by Oreopoulos and Rossow (2011).

The DR method classifies cloud observations based on meteorological information. For example, Bony et al. (2004) link cloud types and cloud radiative forcing in the tropics to the large-scale vertical motion of the atmosphere using the pressure vertical velocity at 500 hPa (ω_{500}). The large-scale tropical circulation is then categorized based on different values of ω_{500}. A number of studies have followed this approach, such as Su et al. (2008) and Li et al. (2014). Others have used a combination of vertical velocity and lower tropospheric stability (LTS; Medeiros & Stevens, 2011; Nam & Quaas, 2013).

Nam and Quaas (2013) found that the identification of low-level cloud using a DR approach is insufficient to distinguish between stratocumulus and shallow cumulus clouds using spaceborne radar observations. They also show that the use of regional subsets are better for the evaluation of low-level clouds in CloudSat data. However, they also identified that regional subsets derived from the DR approach have quite different radar reflectivity histograms. This implies that within a given large-scale environment very different reflectivity profiles can be observed, which highlights the inherent assumption in the DR approach. Another assumption, identified by Nam and Quaas (2013) and Gryspeerdt et al. (2017), is that the reanalyses used are representative of the true atmospheric state.

To be complete, it is relevant to identify that other methodologies have been used to classify clouds based on dynamics. For example, Lau and Crane (1995) and Field and Wood (2007) have used the cyclone compositing technique which places observations and model output into a coordinate system defined relative to low pressure centers. Another approach is to aggregate cloud observations based on objectively determined atmospheric states, this technique was used in Marchand et al. (2009) which compared hydrometeor (cloud and precipitation) occurrence profiles observed by a vertically pointing millimeter-wavelength cloud radar with similar profiles obtained from a combination of a climate model and the QuickBeam radar simulator

(Haynes et al., 2007). More recently, Jolly et al. (2017) composited CloudSat/Cloud-Aerosol Lidar and Infrared Pathfinder Satellite Observations data based on a previously defined synoptic states (Coggins et al., 2014). Chen and Del Genio (2009) also examined CRs relative to various stages of the Madden-Julian Oscillation.

Combinations of the CR and DR methodologies and the use of both viewpoints are rare, but have recently received attention in Williams and Bodas-Salcedo (2017). Gryspeerdt et al. (2014) also used a CR approach to examine aerosol-cloud interactions, but added an extra step to ensure that meteorological covariation was reduced. Recently, Gryspeerdt et al. (2017) combined elements of the CR and DR approaches to develop a classification of cirrus and other high cloud, using a combination of satellite and reanalysis data. Examination of the Cloud Radiative Effect (CRE) for each of the regimes used in Gryspeerdt et al. (2017) indicates that the regimes are not as distinct radiatively as regimes defined using joint histograms (Oreopoulos et al., 2016), with significant variation within the regimes. Interestingly, Oreopoulos et al. (2017) used a CR approach, but then further separated observations based on aerosol optical depth to examine aerosol-cloud interaction mechanisms.

This study examines the level of overlap between the CR and the DR approaches statistically. We also determine the relative merit of the two approaches in understanding cloud properties. With this goal in mind, we update a CR analysis detailed in McDonald et al. (2016) which applied the Self-Organizing Map (SOM) scheme to ISCCP observations. We also apply the same clustering methodology to ERA-Interim pressure vertical velocity profile data to produce a DR. We also assess the level of variability within the CR and DR classifications using a common intracluster variability measure and examine the level of variation within particular cluster members relative to the variation across the SOM. We then compare the results of these two classifications using a contingency table analysis to determine their association. Finally, we composite independent data from the ISCCP FD and CloudSat data sets using our CR and DR classifications to examine the two classifications.

2. Data Sets

We apply the SOM methodology to the ISCCP D1 data set and synchronous ERA-Interim pressure vertical velocity profiles to form independent cloud and DRs which are then intercompared. Details of the ISCCP data set and its derivation are discussed in Rossow & Schiffer (1991, 1999). The ISCCP D1 data set occurs at 3-hourly temporal resolution on a 280- by 280-km equal area grid (6,596 of these grid points cover the Earth) over the period July 1983 to December 2009. For each grid box, the number of cloudy pixels (each pixel is approximately 5 by 5 km) that belongs to one of seven pressure levels and six optical thickness categories is identified. Thus, all cloudy pixels in a grid box are placed in 1 of 42 bins forming a joint histogram of the cloud optical depth versus cloud top pressure. The summation of the cloud fraction in each bin allows the calculation of the total cloud cover (TCC). The ISCCP retrieval of optical depth utilizes visible wavelengths, and therefore the histograms are only available during daylight. Limitations of the algorithms and input data sets used in the ISCCP climatology introduce uncertainties in cloud top pressure in situations with optically thin or multiple-layer clouds present.

ISCCP FD data (Y. C. Zhang et al., 2004) are used to provide clear and overcast radiative outgoing fluxes for the same period at identical spatial and temporal resolution. The outgoing radiative fluxes are derived using a broadband radiative transfer code which takes the ISCCP retrievals of cloud properties and surface albedo as inputs. From the clear and overcast radiative fluxes, we derive the CRE using the formulation defined in Oreopoulos and Rossow (2011):

$$CRE_{SW/LW} = CF[F_{SW/LW}(clr) - F_{SW/LW}(over)], \quad (1)$$

where the outgoing fluxes (F) at the top of the atmosphere in the shortwave (SW) and longwave (LW) are differenced between clear (clr) and overcast ($over$) conditions and multiplied by the cloud fraction (CF).

We also use data from CloudSat (Stephens et al., 2008) which is one of the satellites which forms the NASA *A-Train*, a constellation of satellites with identical orbits that pass over the same parts of the Earth within a narrow time window. CloudSat carries a millimeter-wavelength (94 GHz) cloud profiling radar with a vertical resolution of 240 m and a sea-level footprint of 1.4×1.7 km. It detects hydrometeors within clouds while also penetrating through optically dense upper layers to detect layers at lower altitudes, however studies have shown that it struggles to resolve cloud below 1 km due to ground clutter (Mace et al., 2009). In particular,

this study uses the 2B-GEOPROF R04 (2BG4) to examine the vertical distribution of cloud occurrence. In particular, the 2BG4 product contains calibrated radar reflectivity values and a hydrometeor detection mask that indicates which radar resolution volumes contain hydrometeors (Mace et al., 2009).

This study also employs 6-hourly output from the ERA-Interim reanalysis (Dee et al., 2011) on a 0.75° latitude/longitude grid. These data are then resampled to a 2.5° by 2.5° grid to allow direct comparison with the ISCCP data once it has been reprojected from an equal area grid using a nearest neighbor interpolation scheme. The CloudSat data are also integrated over the same 2.5° by 2.5° grid to produce consistent sampling for intercomparison. We have also resampled the ISCCP data sets to the 6-hr temporal resolution of the reanalysis to ensure consistency.

3. Self-Organizing Maps

SOMs are an iterative unsupervised learning scheme commonly used to reduce the dimensionality of a data set by clustering (Kohonen, 1990). The learning process adjusts a set of reference vectors based on the differences between the reference vector and each input record. A learning rate determines how the adjustment is related to the difference between the reference vector and the input data. Training then consists of many iterations of reference vector adjustment until stable values are reached. In each iteration, the best matching reference vector is identified, using the Euclidean distance, for each input record and updated to more closely resemble the input data.

The learning rate and width of the kernel are reduced as a function of time such that the SOM evolves more quickly initially. The Euclidean distance term associated with the radius vectors for different node is used to identify reference vectors within a certain range of the best matching vector. The vectors that fall within this neighborhood are then updated, although to a lesser degree than the best matching node, this feature of the scheme producing the coherent organization of output. The training process ultimately produces reference vectors that each represent a distinct portion of the multidimensional input space. Training of the neural network is unsupervised with the user specifying only the size and shape and the training parameters; the end result is an objective set of distinct maps (referred to as nodes from this point on) that are representative of the entire data set. The patterns displayed are independent of the initialization process and consistently result from the scheme with some very minor differences based on repeated analysis.

4. Results

4.1. CR Analysis

Figure 1 displays the representative joint histograms identified via application of the SOM technique to a 6-hourly subset of all the daytime histograms from the ISCCP D1 data set observed globally between 2007 and 2008 for regions with topography below 1,000 m above sea level. The representative histograms are the mean histogram derived from all of the specific cases assigned to that node by the SOM scheme. Note that the altitude mask was not used in the earlier work detailed in McDonald et al. (2016). The color-coded bins in Figure 1 identify the cloud fraction within each cloud top pressure/cloud optical depth bin. The relative frequency of occurrence (RFO) and the TCC associated with each node are also identified. After testing various configurations and examining ancillary information, such as the geographical and seasonal distribution of the various states and ERA-Interim reanalyses data to identify whether the corresponding vertical velocity profiles were well ordered, a 5×3 SOM was again selected to be optimal as previously used in McDonald et al. (2016). The 5×3 grid displays sufficient intercluster variability while maintaining relatively high frequencies for each cluster and, we will show later, displays slightly smaller intracluster variability than the classification identified in McDonald et al. (2016). A Sammon map (Sammon, 1969) was also produced which displayed a gridded structure with some minor distortion and no twists (not shown) which is a good indication that the SOM was well constructed and trained. To further test the robustness of the number of nodes in the SOM, the correlation coefficients between the different geographical patterns related to each node were also derived (not shown). Using the 0.8 correlation coefficient threshold from previous studies (McDonald et al., 2016; Tselioudis et al., 2013), the nodes in the 5×3 SOM are all distinct.

The set of patterns represented in Figure 1 are very similar to those presented in Figure 1 of McDonald et al. (2016) apart from the top left hand corner of the SOM. Similar to the SOM pattern detailed in McDonald et al. (2016), we find that the top left node in the current SOM (node I1) is predominantly related to clouds with high tops (low pressure) and moderate to high optical depths and that the bottom right node in the grid

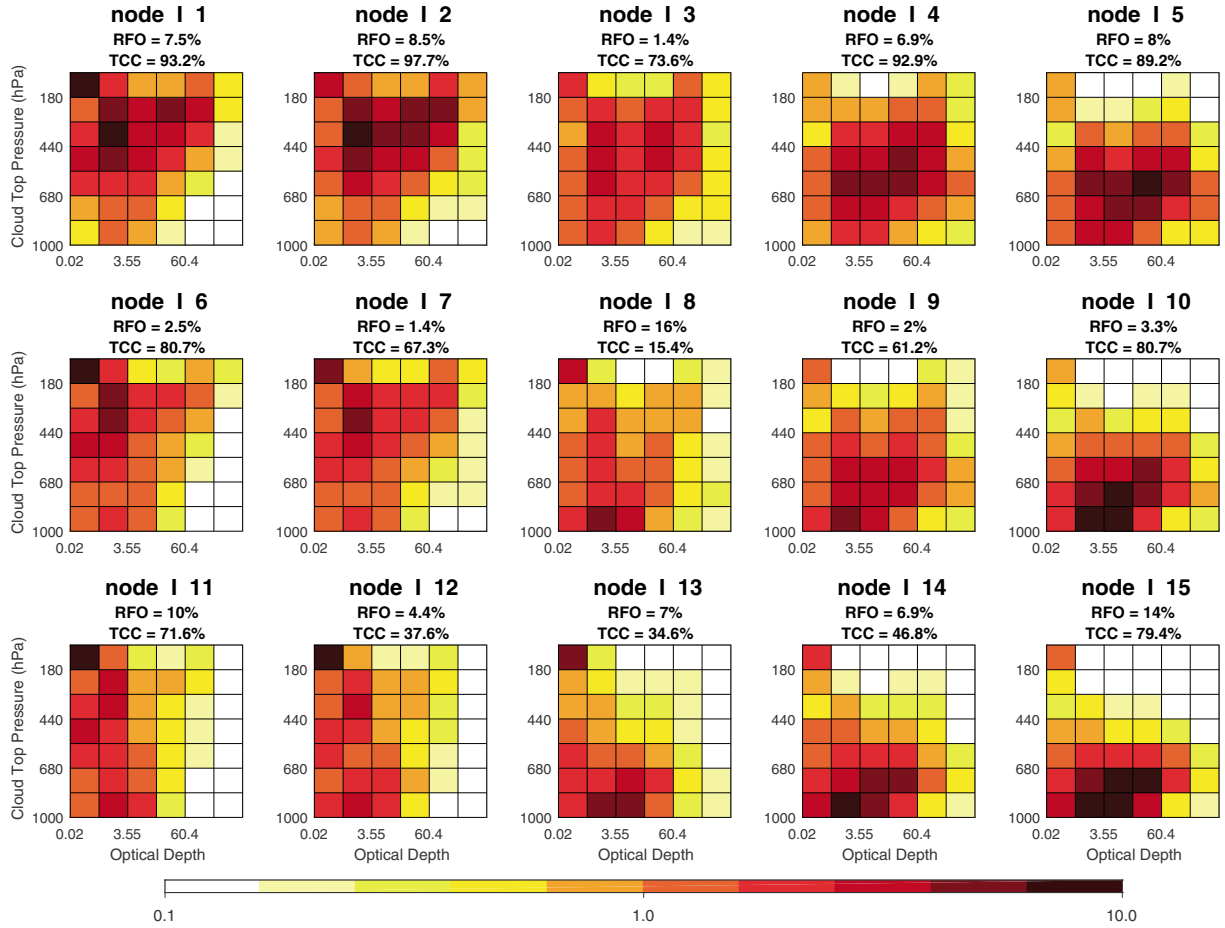

Figure 1. The SOM reference vectors displayed as joint histograms of cloud optical depth versus cloud top pressure, representing the 15 nodes derived by the application of the SOM to International Satellite Cloud Climatology Project observations. The relative RFO and the TCC associated with each node in the SOM is indicated in the legend above each histogram. Note the logarithmic color scale. SOM = Self-Organizing Map; RFO = relative frequency of occurrence; TCC = total cloud cover.

(node I15) is related to low-level (high cloud top pressure) clouds with low to medium optical depths. Thus, polar opposites in terms of cloud top pressure are observed at the ends of this diagonal. We also observe that the cloud top pressure for the highest occurrence states increases from left to right in the grid, while the optical depth decreases from top to bottom in the grid in a similar manner to that observed in the 5 × 3 SOM displayed in McDonald et al. (2016). The nodes at the four corners of the 5 × 3 SOM (I1, I5, I11, and I15) and node I2 and I8 have the highest RFOs. We demonstrate that the difference observed between the current SOM and that detailed in McDonald et al. (2016) represents a refinement of the previous classification. One reason for the difference between the current SOM and the one displayed in McDonald et al. (2016) appears to be associated with the longer period examined. However, the removal of histograms based on the altitude mask appears more important. These criteria remove possible artifacts over about 7.5% of the Earth surface from consideration with the excluded regions primarily confined to Antarctica, Greenland, and the Himalayan plateau.

To further examine the representativeness of the SOM nodes, we compute the Pearson correlation coefficient between each node and all the individual joint histograms assigned to that node. Figure 2 displays the distribution of these correlations for each node. A similar procedure has been used previously in synoptic climatology studies by Feldstein and Lee (2014) and Gibson et al. (2017) to measure intracluster similarity. Figure 2a displays the pattern correlations for the SOM nodes displayed in Figure 1 assigned using the Euclidean distance between the SOM pattern and the 42 element vector of cloud amount for the joint histogram. Figure 2b displays the pattern correlations for the SOM nodes shown in Figure 1 in McDonald et al. (2016) assigned using the same methodology. Comparison of Figures 2a and 2b shows that the median values

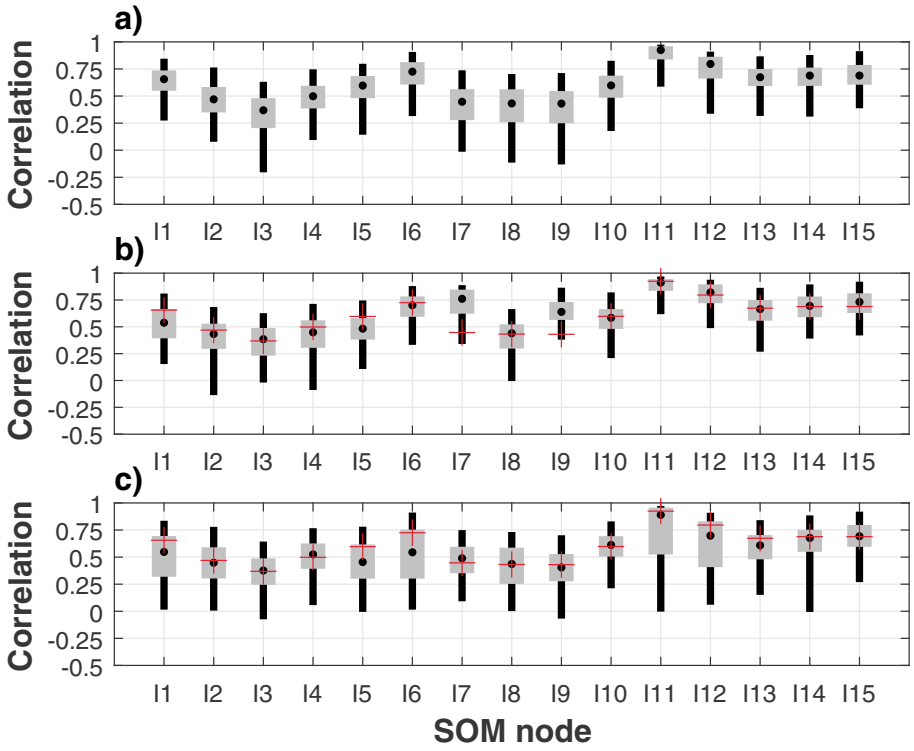

Figure 2. Boxplots of Pearson correlations between representative patterns derived using the SOM methodology and all the individual joint histograms assigned to these patterns. (a) represents the correlations between the SOM reference vector displayed in Figure 1 and all the joint histograms assigned to that node based on Euclidean distance. (b) represents the correlations between the SOM reference vector displayed in McDonald et al. (2016) and all the joint histograms assigned to that node based on Euclidean distance. (c) represents the correlations between the SOM reference vector displayed in Figure 1 and all the joint histograms assigned to that node based on the scheme detailed in Williams and Webb (2009). Titles for each panel identify the lower and upper quartiles and the median for all nodes/states. To enhance comparison, panels (b) and (c) include red crosses representing the median values displayed in panel (a). SOM = Self-Organizing Map.

of the Pearson correlation distributions for the current SOM are similar or larger than those derived from the SOM nodes identified in McDonald et al. (2016) for all the high RFO nodes apart from node I15 (I1, I2, I4, I5, I8, I11, I13, and I14), while reductions in the median correlation coefficient for the new SOM are observed for nodes I3, I7, and I12 which all have low RFO and are therefore less critical. This implies that the new SOM has put less significance on nodes that represent transition states, a potential extra benefit. The median and lower and upper quartiles derived across all nodes suggest that the current classification has higher intracluster similarity than that for the SOM detailed in McDonald et al. (2016), supporting our view that the current SOM is a slight refinement. In an attempt to further improve our classification, we also examined whether the assignment method detailed in Williams and Webb (2009) which uses the total cloud fraction and normalized values of the mean cloud optical depth and cloud top pressure in the Euclidean distance assignment metric produced a noticeable change in allocations. We found that the 42 vector Euclidean distance metric (see Figure 2a) was preferable to the technique detailed in Williams and Webb (2009; see Figure 2c) when judged using this intracluster similarity metric. In particular, very low correlations between the node patterns displayed in Figure 1 and individual joint histograms assigned using the Williams and Webb (2009) technique occurred more often than the direct technique.

The geographical distribution of the RFO for each node in the SOM is shown in Figure 3 and displays significant similarities with Figure 3 in McDonald et al. (2016), this being particularly clear for nodes in the bottom row of the SOM (I11 – I15). Nodes I14 and I15 are both related to marine stratocumulus and stratus cloud decks as in McDonald et al. (2016), with node I14 very similar to the open mesoscale cellular convection class identified in Muhlbauer et al. (2014) and node I15 connected to their closed mesoscale cellular convection class. One of the weaknesses of the SOM technique detailed in McDonald et al. (2016) is that they form a gridded

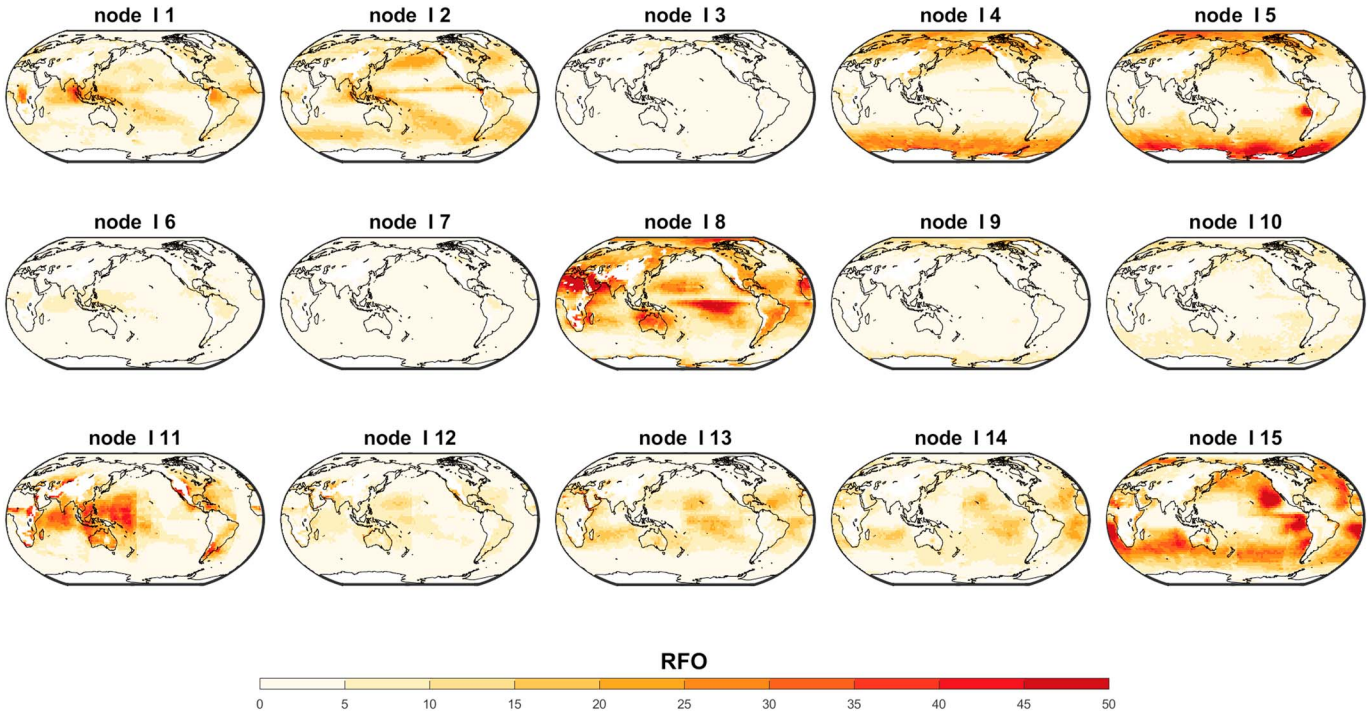

Figure 3. Geographic maps of the annual mean RFO (%) of the cloud types linked to the 15 nodes identified by the Self-Organizing Map displayed in Figure 1. RFO = relative frequency of occurrence.

representation of a continuous data space which can sometimes cause data sparse regions to be represented more strongly than in other clustering techniques. Nodes potentially related to transitions constitute a smaller total percentage of the data than in McDonald et al. (2016; c.f. nodes 4, 6, 10, and 12 in McDonald et al., 2016, with I3, I10, and I12 in the current CR).

Another problem identified in McDonald et al. (2016) was that node 1 represented a mix of histograms connected to WS 1 to 3 from Tselioudis et al. (2013). This is problematic because these WSs relate to distinct physical regimes (Tan et al., 2013; Tselioudis et al., 2013). The current SOM-derived CR separates high-level clouds more effectively. In particular, the geographical pattern of node I1 displayed in Figure 3 bears a strong resemblance to WS 3 in Tselioudis et al. (2013), while the node I2 geographical structure appears to be similar to WSs 1 and 2. WS 1 in Tselioudis et al. (2013) represents regions dominated by tropical deep convection and cold frontal convection in the storm tracks, with WS 2 representing optically thicker clouds and lower top heights almost exclusively associated with the midlatitude storm tracks. Tselioudis et al. (2013) identify that WS 3 is dominated by high clouds of low to medium optical thickness that have higher cloud tops but have a similar geographical distribution to WS 1. The close geographic association of WS 3 with tropical convection indicates it represents the stratiform anvil clouds associated with mesoscale convective systems, cirrus cloud, and some mixed isolated less organized and weaker convective cloud.

While overall our analysis shows the superiority of the new CR compared to that in McDonald et al. (2016), close examination of Figure 3 also highlights an interesting problem with the CR formed. In particular, for node I11 a linear feature is observed around the international dateline and after analysis this appears to be associated with the fact that the ISCCP information in this region is derived from two different satellite instruments, namely MTS-1 and GOES-11 for the 2007–2008 period examined. Thus, the classification appears to highlight a difference in the joint histograms from the two satellites. Marchand et al. (2010) have previously identified that the sensitivity of satellite retrievals to multilayer clouds where the upper layer is optically thin can produce significantly different joint histograms for different satellites. In particular, they identified that ISCCP retrieves a cloud top height that is frequently biased into midlevels, whereas MODIS usually identifies the upper-level cloud and MISR the lower cloud top. We believe that the different satellites derivation of the joint histogram is the problem in this case because the ISCCP FD data set does not display this discontinuity and this data set includes information from the lower-level data set. This means that the radiative patterns associated with

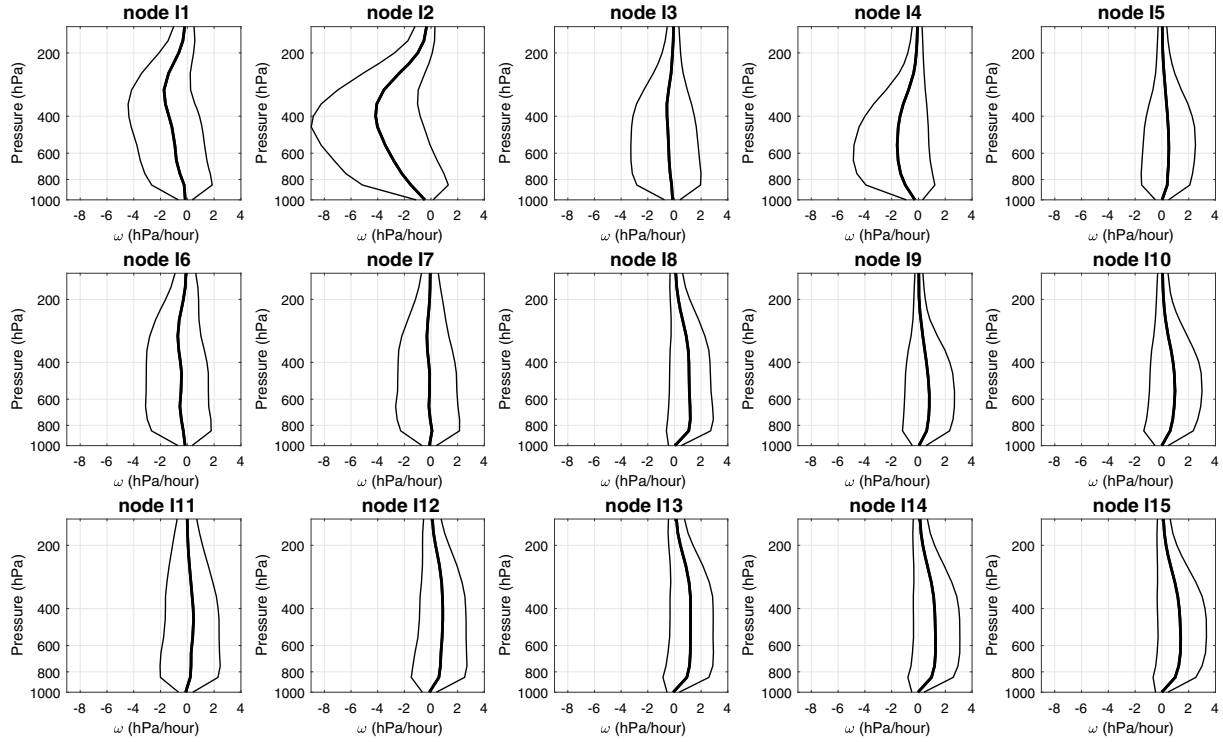

Figure 4. The median (thick black line) and interquartile ranges (thin black lines) for the vertical profiles of the pressure vertical velocity (hPa/hour) for each node in the Self-Organizing Map. Negative values correspond to ascending motion and positive values to descending motion.

the different patterns are rather similar. We should also identify that an examination of the previous CR in McDonald et al. (2016) and the WSs detailed in Tselioudis et al. (2013) shows a similar discontinuity (not shown) in WSs 5 and 6 for this period.

To test the utility of the new SOM, we create composite median vertical velocity profiles in Figure 4. Similar to results in McDonald et al. (2016), we find that the various SOM nodes display a distinct structure with a shift from profiles dominated by positive (descent) to negative (ascent) pressure vertical velocities as we move from right to left in the SOM (see Figure 4). The top left node in Figure 9 in McDonald et al. (2016) was predominantly related to large negative pressure vertical velocities (connected to upward motion) with a maximum value at around 400 hPa and was associated with clouds with high cloud tops. The bottom right node in McDonald et al. (2016) was related to positive vertical velocities throughout the profile and was therefore linked to a region of strong descent and low-level clouds. A gradual shift from positive (descent) to negative (ascent) vertical velocities moving from right to left in that SOM structure was also clear. These characteristics are largely reproduced in the refined ISCCP classification. The most obvious difference between the patterns is that node I1 is no longer related to the highest ascent rates, which are now connected to node I2. This makes sense when we consider that the WS in Tselioudis et al. (2013) roughly corresponding to node I1 represents a mixture of the stratiform anvil clouds portions of mesoscale convective clouds and cirrus cloud. This feature also corresponds with results in Tselioudis et al. (2013) which showed that these clouds were connected to upward motion, but were not connected to the highest upward vertical velocities. Node I2 in Figure 4 is therefore connected to the largest negative vertical velocities (highest ascent rates) which also show correspondence with the patterns in Tselioudis et al. (2013; WSs 1 and 2). Thus, the ordering of Figure 4 is physically meaningful. Interestingly, while the joint histograms and geographical distribution of the occurrence frequency for nodes I4 and I5 are rather similar, the vertical velocity profiles are quite well separated which highlights that this subtle variation in Figure 1 is connected to meteorological state.

Leinonen et al. (2016) identified that there can be significant variability within specific clusters in a CR which is linked to the different clusters representing different types of clouds in different regions. Regional radiative differences between ISCCP WSs were also highlighted by Oreopoulos and Rossow (2011) and suggest this might be a universal feature of CRs. Leinonen et al. (2016) hypothesized that this results from the variable

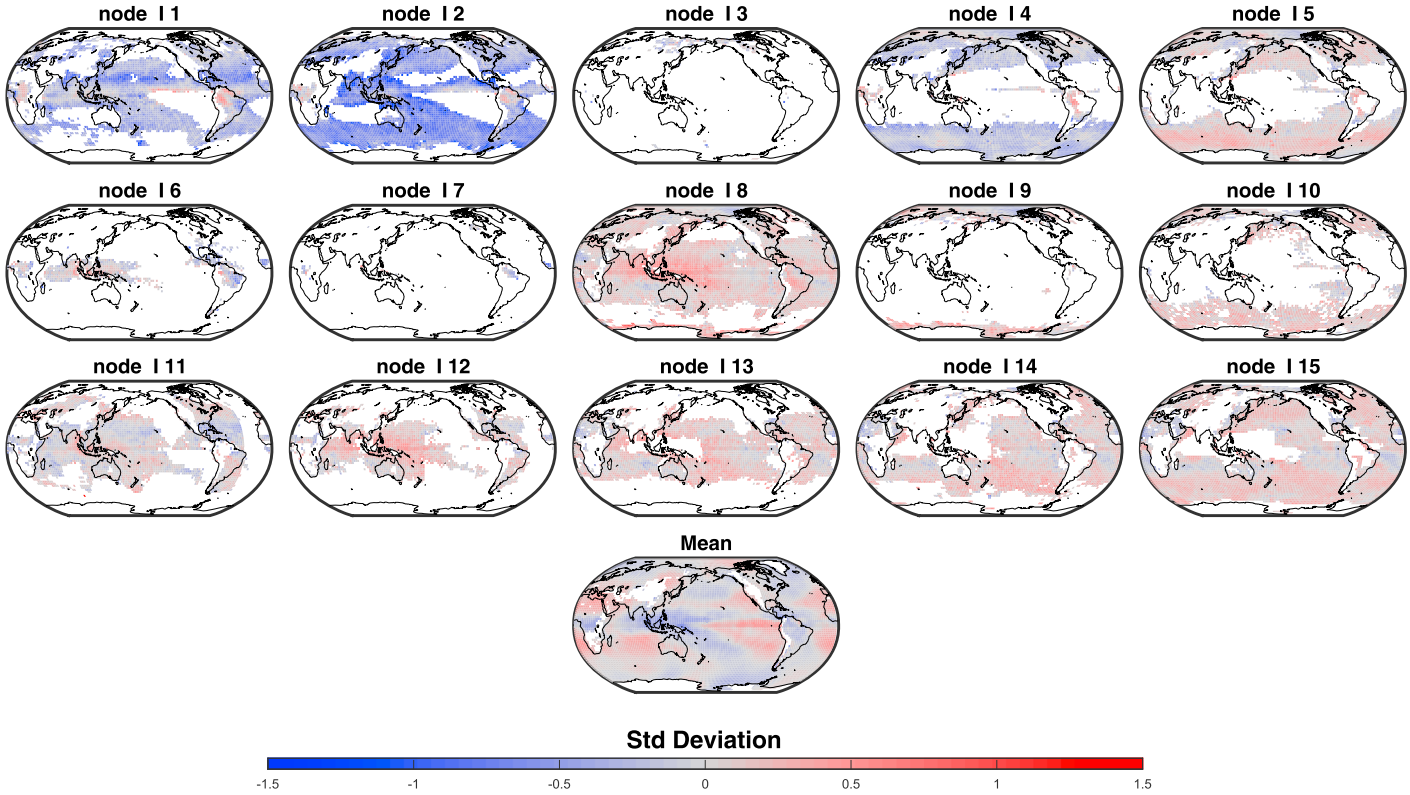

Figure 5. Geographic maps of the mean anomaly pressure vertical velocity at 500 hPa normalized by the standard deviation for the 15 nodes identified by the Self-Organizing Map displayed in Figure 1 and the mean pressure vertical velocity for the period 2007 to 2008 inclusive, again normalized by the standard deviation. Regions where the relative frequency of occurrence of the node is below 5% are not displayed to improve clarity.

meteorological environments producing different cloud structures, which nevertheless have similar signatures in passive measurements. To examine their hypothesis, we display maps of the mean anomaly pressure vertical velocity at 500 hPa normalized by the standard deviation for each node in the SOM (see Figure 5) to determine whether the variability displayed in Figure 4 is related to regional differences. Inspection of Figure 5 shows very clear ordering with the global pattern dominated by large negative vertical velocity anomalies in node I1 and large positive vertical velocity anomalies for node I15. However, within each node notable variability across the globe does exist. In particular, the largest negative vertical velocity anomalies in node I2 occur over the ocean in the Pacific warm pool, the South Pacific and South Atlantic convergence zones, and the Indian Ocean, with weaker negative vertical velocity anomalies over the midlatitude storm tracks. For nodes I14 and I15, regional variability means that stronger positive vertical velocities (subsidence) occur over the tropics and near zero velocity anomalies are observed at higher latitudes. These results support the proposition that regional variability is partially determined by changes in the meteorological environment. The fact that there are distinct geographical structures in each nodes, map further supports this claim.

4.2. DR Analysis

We have previously identified the relationship between ERA-Interim pressure vertical velocity profiles and CRs derived via application of the SOM technique to the ISCCP D1 data set (see Figure 4). In addition to this approach, research has characterized cloud systems based on DRs under the assumption that they influence cloud formation. Oreopoulos et al. (2017) identify that ω_{500} is a commonly used meteorological indicator of the dynamic state of the atmosphere, but that work examined full profiles of ω to be thorough. We therefore take this idea a step further and apply the SOM technique to pressure vertical velocity profiles from ERA-Interim reanalyses. Given that studies have shown the importance of LTS for low-level cloud (Klein & Hartmann, 1993), we could also have used this variable (among others) in our cluster analysis. However, we choose to form our DR using only variations in the pressure vertical velocity. This decision is partly associated with the distinct changes in this variable for different cloud types identified in McDonald et al. (2016), but also because the use of a mixture of meteorological variables in a SOM framework introduces an inherent assumption. In particular,

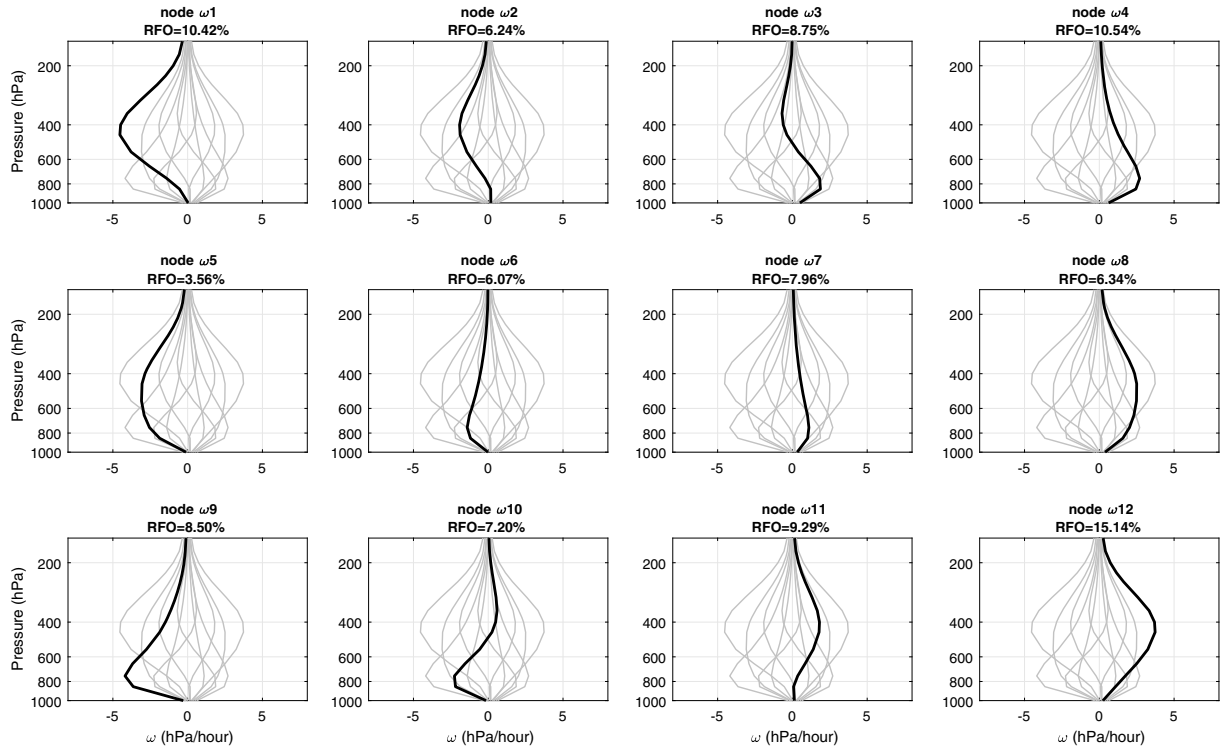

Figure 6. The dynamical regime SOM reference vectors displayed as vertical profiles of the pressure vertical velocity (hPa/hour) for each node in black, and gray lines identify the vertical velocity profiles connected to all the other nodes for reference. These patterns represent the 12 dynamic regime nodes identified by the SOM technique applied to the ERA-Interim pressure vertical velocity data. The RFO associated with each node in the SOM is indicated in the legend above each histogram. Note that negative values correspond to ascending motion and positive values relate to descending motion. SOM = Self-Organizing Map; RFO = relative frequency of occurrence.

the common practice of normalization of all inputs into a multivariate SOM effectively introduces the assumption that the various variables are of the same importance. Applying a weighting scheme to address the normalization bias would also require the precise nature of the relative importance of the different variables to be known which is clearly a difficult task for the wide range of cloud types examined. McDonald et al. (2016) also display less consistency between the LTS and the total columnar water vapor to specific nodes, though studies such as Jiang et al. (2012) and Su et al. (2013) have shown the strong relationship between moisture metrics and CRs. We also note that work detailed in Nam and Quaas (2013) suggests that a multiparameter scheme may not improve the relative quality of the results. In particular, Nam and Quaas (2013) found that the identification of low-level cloud using a DR approach using vertical velocity and LTS is insufficient to distinguish between stratocumulus and shallow cumulus clouds. Additionally, work detailed in Taylor et al. (2015) used both ω_{500} and LTS to identify atmospheric state regimes, but still observed significant regional variability in cloud properties within each regime. This suggests that a wide range of dynamic or thermodynamic variables are likely required, and for the sake of simplicity we choose to only use the pressure vertical velocity profile in the current study. This means that this study will not be definitive, but it allows us to define a methodology that can be used for later more comprehensive analyses.

Figure 6 displays characteristic profiles of the pressure vertical velocity derived from 6-hourly global output for the 2007 and 2008 calendar years for regions with topography below 1,000 m above sea level using the SOM technique. These factors were selected to ensure identical sampling to that used in the CR analysis. Testing of various configurations and examining ancillary information, such as the geographical distribution of the various states, the Sammon map of the SOM (not shown) and the correlations between the geographic RFO maps for the different nodes suggest that the 5 × 3 SOM used for the CRs is not optimal in this case. In particular, individual nodes within the 5 × 3 SOM have correlations above the 0.8 threshold used in previous studies. This suggests that the vertical velocity profiles contain less independent information than the ISCCP joint histograms, this likely identifies that the simple DR scheme derived cannot be as helpful a classification. This lack of independence means that we use a 4 × 3 SOM for the vertical profiles of pressure vertical

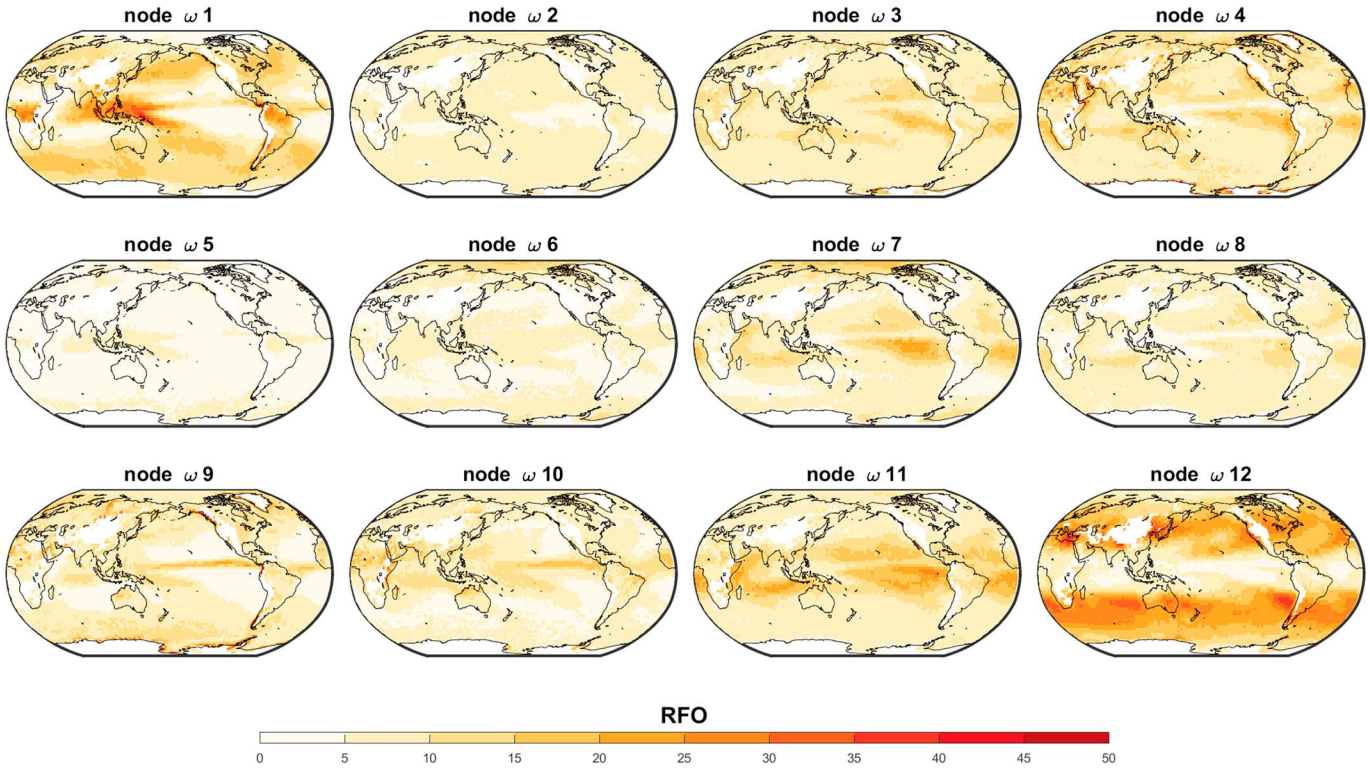

Figure 7. Geographic maps of the annual mean RFO (%) of the vertical velocity profiles linked to the 12 dynamic regime nodes identified by the Self-Organizing Map displayed in Figure 6. RFO = relative frequency of occurrence.

velocity to optimize the DR analysis. An analysis using a 5×3 SOM might have been more directly comparable to the CR, but disadvantages the statistical analysis of the DR scheme and thus was not considered. Examination of Figure 6 shows that the most negative vertical velocities (linked to ascent) occur in the left hand column of the SOM and that the most positive vertical velocities (linked to descent) occur in the right hand column of the SOM. Comparison of node ω1 (top left) and node ω12 (bottom right) shows they are near mirror images with the largest magnitude vertical velocities occurring at around 400 hPa. The lowest magnitude vertical velocities occur in the center of the SOM grid. Profiles with their highest magnitude positive and negative vertical velocities at higher pressures (near 800 hPa) are observed in the top right (node ω4) and bottom left (node ω9) of the grid, respectively. The SOM grid therefore displays a distinct ordering, as expected using this methodology.

Figure 7 displays the geographical distribution of the RFO of the DR nodes. Figure 7 shows some similarities with the patterns displayed in Figure 1, for example, node ω1 in the ERA-Interim derived SOM (node ω1 in Figure 7) looks rather similar to that for node I1 or node I2 in the ISCCP derived SOM (see Figure 1) around the tropics. This relationship highlights that regions of ascent are observed predominately in the regions where convection occurs commonly. Similarly, the regions of subsidence in Figure 7, linked to the rightmost column in the SOM, are preferentially related to regions in Figure 1 linked to low-level cloud.

To quantify the relationship between cloud observations and the DR classification, the mean ISCCP joint histograms composited based on assigning data to the DR nodes are displayed in Figure 8. Figure 8 exhibits a clear ordering with the top left node in the SOM (node ω1) linked to clouds with high tops (low pressure) and moderate to high optical depths and the bottom right node in the grid (node ω12) related to low-level (high cloud top pressure) clouds with low to medium optical depths. This structure is quite similar to the CR pattern observed in Figure 1. Though, the absence of a clear-sky state is notable with the lowest cloud cover being associated with node ω11 at 56.1%. The ordering in Figure 8 suggests that the vertical velocity profile is an important determinant of the cloud top pressure as might be expected. Examination of the mean TCC for each node for the DR classification identifies a much smaller range of values than that for the CR. Inspection indicates that this results from very high cloud covers and clear skies being mixed in with the overall tendency. The standard deviation of the bins in each joint histogram (not shown) also displays much higher values than

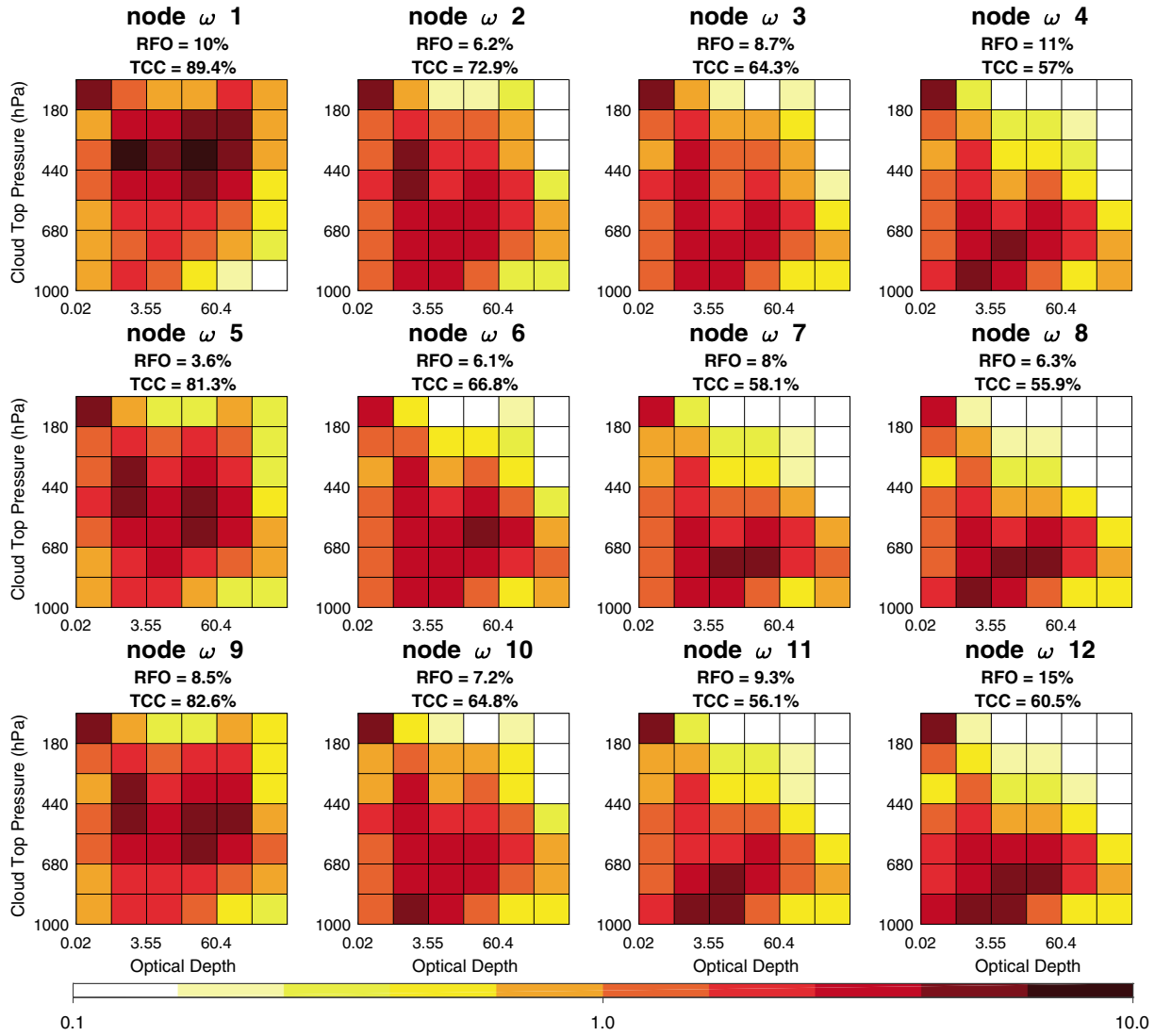

Figure 8. International Satellite Cloud Climatology Project joint histograms of cloud optical depth versus cloud top pressure, representing the 12 nodes identified by the Self-Organizing Map shown in Figure 6. The RFO and the TCC associated with each node in the Self-Organizing Map is indicated in the legend above each histogram. Note the logarithmic color scale. RFO = relative frequency of occurrence; TCC = total cloud cover.

those related to the CR (also not shown). This is unsurprising as we know that many factors influence cloud formation. However, if vertical velocity was a key determinant of cloud structure, it would theoretically be more efficient to classify on that variable than to classify on the cloud data. Thus, while our analysis suggests that the DR scheme can be used to composite specific cloud characteristics, there appears to be a greater ambiguity in this classification than using a CR classification. This ambiguity likely reflects the inherent assumptions connected with classifying cloud using the DR approach.

We inspect the intracluster similarity of the DR by computing the correlation between the mean joint histograms displayed in Figure 8 and all the individual joint histograms assigned to that node. Figure 9a displays the distribution of these pattern correlations for each node, examination shows that the median values for the DR SOM are always below 0.5 and the median value for all nodes is 0.37. These values are smaller than those for the CR classification shown in Figure 2. To ensure that the clustering is not at fault, Figure 9b displays the correlation between the representative pressure vertical velocity profiles (shown in Figure 6) and the individual pressure vertical velocity profiles assigned to that node. Examination of Figure 9b proves that the SOM methodology has produced an accurate clustering with high intracluster similarity in each node, with the exception of node $\omega 7$. Thus, the intracluster variability observed when inspecting corresponding cloud data

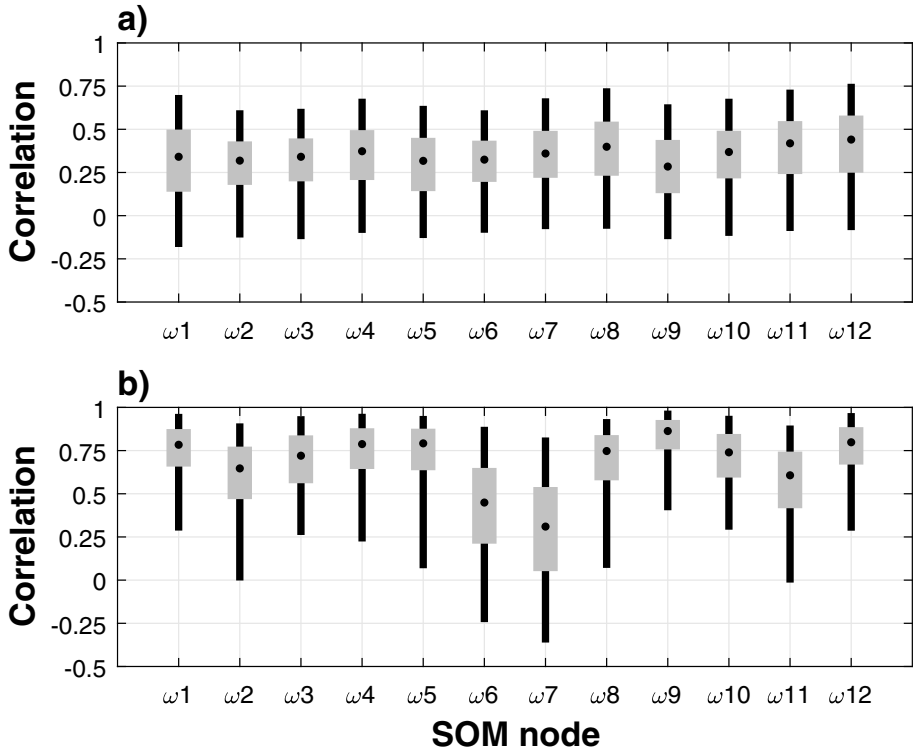

Figure 9. Boxplots of Pearson correlations for representative International Satellite Cloud Climatology Project joint histograms patterns derived using ERA-Interim pressure vertical velocity profiles and all the individual joint histograms assigned to these patterns (a). Similarly, boxplots of Pearson correlations for representative nodes derived from the ERA-Interim vertical velocity profiles patterns relative to individual ERA-Interim pressure vertical velocity profiles. SOM = Self-Organizing Map.

reflects the assumptions connected with the DR classification, namely that cloud formation is only controlled by the pressure vertical velocity profile in this case.

4.3. Contingency Table Analysis

In an effort to determine the level of influence of the meteorological environment on cloud formation and the association between the two classifications, we compare the DR and CR SOMs in a contingency table. The contingency table in Figure 10 allows us to identify which cloud states are most strongly impacted by the pressure vertical velocity profile. The values displayed represent the difference between the number of observations classified in a specific ISCCP and vertical velocity derived node and the expectation value for that combination, defined in Press et al. (1992), divided by the expectation. Thus, red squares represent observations which are more common than the expectation and blue squares represent observations which are less common than the expectation.

Examination of Figure 10 shows that nodes I1–I4 in the CR have higher occurrences than the expectation for the nodes in the left hand column of the DR SOM. This demonstrates that the nodes connected to ISCCP observations with high cloud tops are strongly connected to vertical velocity profiles with high ascent rates. Inspection also shows that ISCCP nodes I1–I4 occurrence rates are significantly lower than the expectation for nodes in the DR classification connected to regions of subsidence (ω8 and ω12). We also find that nodes I13–I15 in the CR are preferentially observed during periods linked to the right hand column of the DR (nodes ω4, ω8, and ω12) suggesting these nodes are strongly related to subsidence. This clearly concurs with results previously reported in Figures 4 and 8. We also find that other nodes in the CR classification, particularly the nodes connected to nodes I7, I8, and I9 are not strongly connected to any specific DR node. Calculation of Cramer's V metric, which varies between zero and one with zero representing no association and one representing perfect association between the two classifications, is 0.16 which represents little association between the CR and DR schemes (Press et al., 1992). Calculation of the dependency also detailed in Press et al. (1992) is

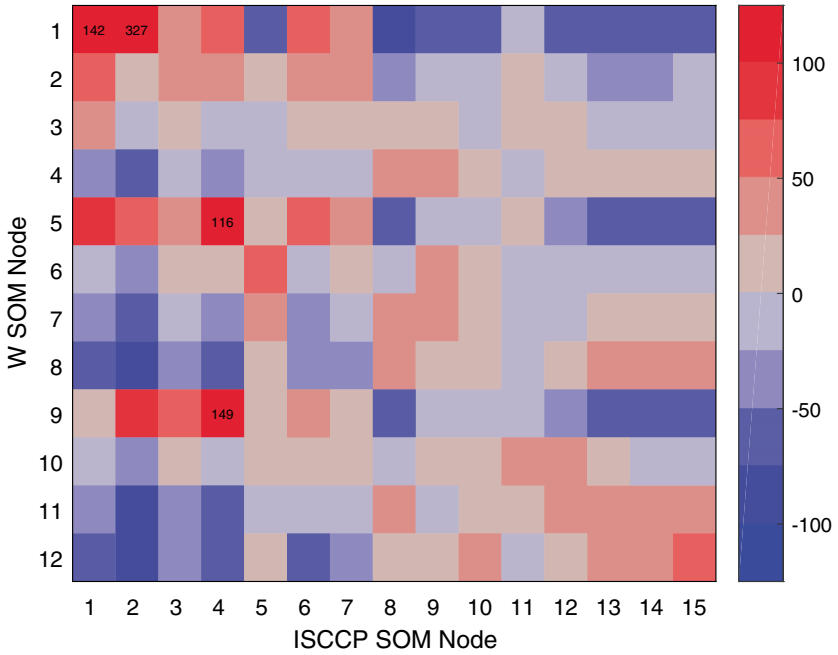

Figure 10. Anomalous relative frequency of occurrence (% relative to that expected) of node combinations for the ISCCP- and ω-derived SOMs. ISCCP = International Satellite Cloud Climatology Project; SOM = Self-Organizing Map.

only 0.0532 which again identifies little association. Therefore, we observe little association statistically which suggests that the dynamic and CRs formed are largely independent.

4.4. CRE Analysis

To test the regional variability in the CR and DR schemes, we display maps of the normalized difference between the mean LW CRE for a particular node at a specific position ($\overline{CRE_{LWn}(\theta,\phi)}$) and the global mean LW CRE, ΔCRE_{LWn}, defined as

$$\Delta CRE_{LWn} = \frac{\overline{CRE_{LWn}(\theta,\phi)} - \overline{CRE_{LWn}}}{\sigma(CRE_{LW})}, \tag{2}$$

where θ is latitude, ϕ is longitude, overbars denote means, $\sigma(CRE_{LW}$ is the global standard deviation of the LW CRE for all nodes, and the n subscript is associated with that node in the classification. The other symbols used are identical to their usage in equation (1). Titles for each panel identify the global mean LW CRE ($\overline{CRE_{LWn}}$) for each node. This variable identifies whether there is a large spread from the ($\overline{CRE_{LWn}}$) across the globe.

The geographic map of ΔCRE_{LWn} for the CR is displayed in Figure 11, the values of LW CRE used in the analysis are calculated from the ISCCP FD data set as detailed in section 2. The global mean LW CRE for the nodes in the CR vary between 5 and 73 W/m^2 in this analysis is quite similar to the range displayed in McDonald et al. (2016). Examination of the distribution of SW and LW CRE for each node (not shown) also displays a rather similar pattern to that shown in Figure 11 of McDonald et al. (2016). Inspection of ΔCRE_{LWn} in Figure 11 shows that the largest regional variability occurs in nodes I1, I2, and I11. These three nodes are all associated with high cloud top cloud and display a strong latitudinal variability which corresponds to lower cloud top pressures (higher altitude cloud tops) at the equator and higher cloud top pressures (lower altitude cloud tops) at midlatitudes. The variability in ΔCRE_{LWn} is small in all the other nodes, but does show some signs of the same latitudinal variation in nodes I4, I5, and I6.

The regional variability identified in nodes I1, I2, and I11 seems likely to be associated with variations within those cloud classes linked to changes in tropopause altitude and has a similar scale to that in Leinonen et al. (2016). There is also some evidence of a relationship between high ascent rates (see Figure 5) and high cloud tops (see Figure 11), for example, in node I2 in the Pacific warm pool. Thus, the CR created from ISSCP D1 data appears to perform well with understandable regional variability in a limited number of nodes. The CR classification also displays little variability in most nodes in LW CRE highlighting a physically meaningful classification which is highly self consistent within most nodes.

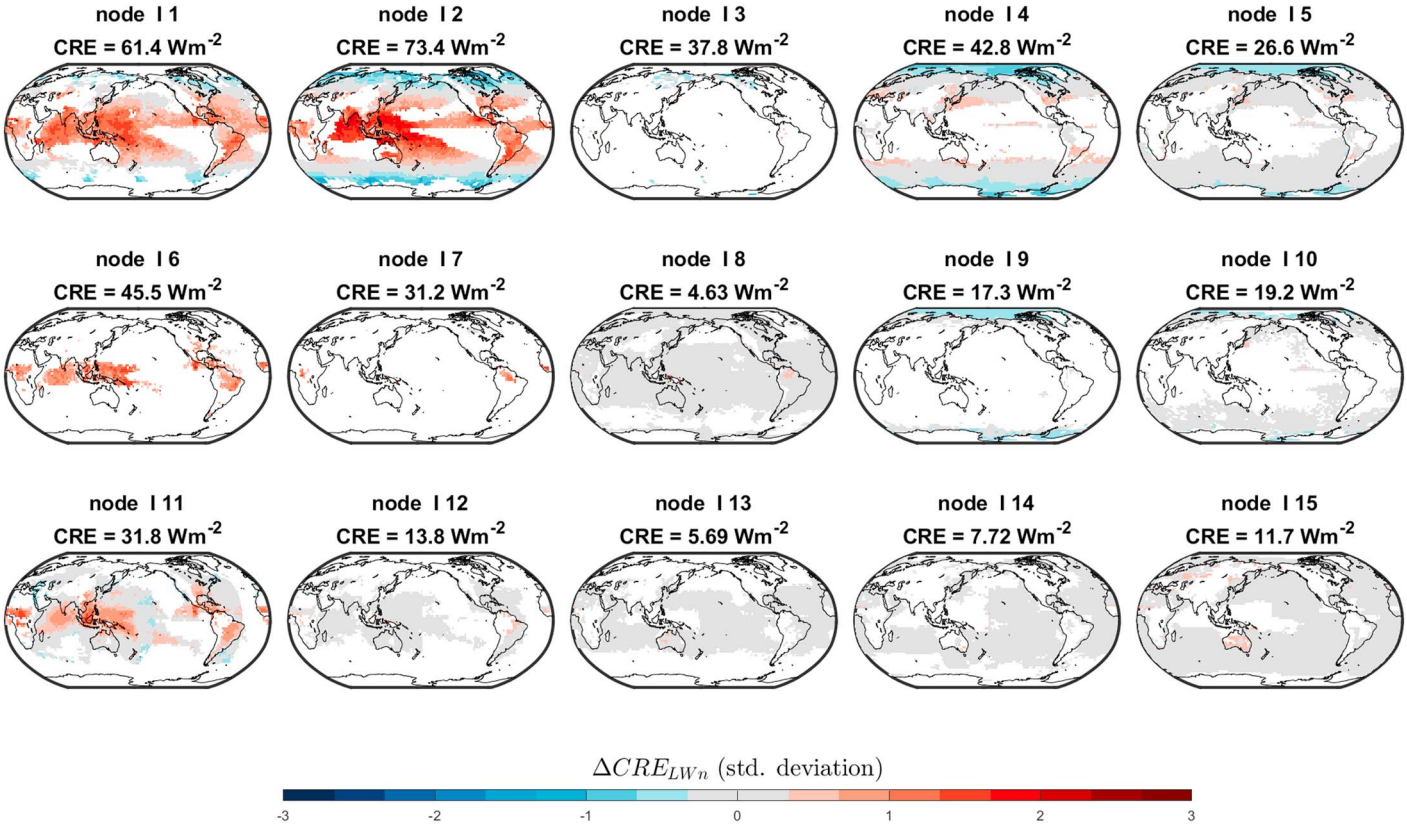

Figure 11. Geographic maps of the normalized difference between the LW CRE for a particular node and the mean LW CRE for all 15 nodes identified by the Self-Organizing Map displayed in Figure 1. Regions where the relative frequency of occurrence of the node is below 5% are not displayed to improve clarity. CRE = Cloud Radiative Effect; LW = longwave.

Geographic maps of the ΔCRE_{LWn} for the DR scheme are displayed in Figure 12. Figure 12 shows significant variability in the ΔCRE_{LWn} measure in nearly every node, with node ω8, ω11, and ω12 displaying the smallest variability. The largest regional variability is observed in nodes ω1, ω5, and ω9 (the nodes in the left hand column of the DR SOM) which are linked to high-level clouds. In comparison to the variability displayed in Figure 11, many more nodes show sizable variations. Note that the geographic maps in Figures 11 and 12 are normalized to the same value of $\sigma(CRE_{LW}$ and are therefore directly comparable. The pattern of the regional variability observed is similar for every node with only the magnitude of the variability changing, this identifies a less focused relationship between the DR derived SOM and the LW CRE metric. Figure 12 is also more complex than that in Figure 11 and appears similar to the mean LW CRE ($\overline{CRE_{LW}}$) suggesting that the DR classification does not separate out LW CRE efficiently.

Geographic maps of the normalized difference between the SW CRE at a specific position for a particular node and the global mean SW CRE are shown in Figures S1 and S2 of the supplementary information. In this case, the range of CRE_{SWn} for the current CR is −24.2 and −238 W/m^2, while for the DR this range is only −34.7 and −77.9 W/m^2. Thus, the nodes in the DR scheme do not appear to show the range observed in previous studies (McDonald et al., 2016; Oreopoulos et al., 2014, 2016). Examination of this metric shows very high variability for nodes I1, I2, I4, I5, and I15 in the CR and sizable, but smaller variability than the CR, in nearly every node of the DR. We interpret this as suggesting a weaker linkage between the CR and SW CRE variations, but almost no linkage between the SW CRE at any specific point and the DR classification.

4.5. CloudSat Analysis

Limitations of the ISCCP data set introduce uncertainties in cloud top pressure in situations with optically thin or multiple-layer clouds. Thus, CRs derived from ISCCP observations may inherently contain biases as identified in work by Chen and Del Genio (2009) and Mace and Wrenn (2013). We examine whether this uncertainty impacts the relative efficacy of the current CR and DR classifications by compositing CloudSat observations assigned to the nodes in those classifications. We construct reflectivity-altitude joint histograms in 2.5° by

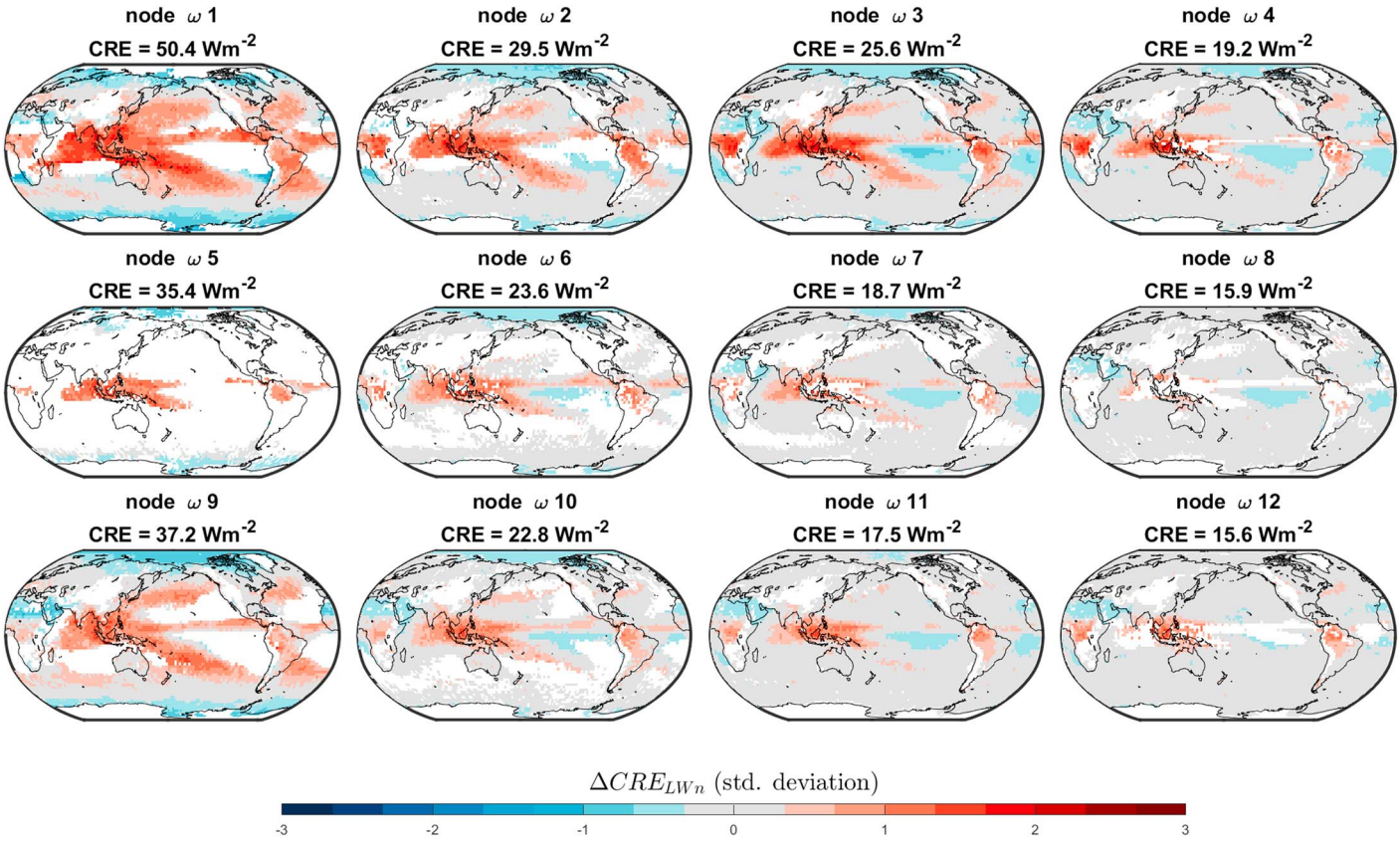

Figure 12. Geographic maps of the normalized difference between the LW CRE for a particular node and the mean LW CRE for all 12 nodes identified by the Self-Organizing Map displayed in Figure 6. Regions where the relative frequency of occurrence of the node is below 5% are not displayed to improve clarity. CRE = Cloud Radiative Effect; LW = longwave.

2.5° latitude-longitude bins using CloudSat observations from 2007. As the ISCCP CRs are only available during the day, the CloudSat observations were also restricted to daytime measurements in order to ensure synchronous observations. We normalize the reflectivity-altitude joint histograms such that the sum of the histogram counts is proportional to the total cloud fraction measured in a similar manner to that detailed in Leinonen et al. (2016). This procedure enables us to distinguish not only between different distributions of reflectivity and altitude, but also between regimes that have similar reflectivity-altitude distributions with different amounts of cloud. These joint histograms were generated using the radar reflectivity data in the 2BG4 CloudSat product (Mace et al., 2009). CloudSat observations were only composited in this analysis when greater than 6 hr of ISCCP D1 data or ERA-Interim output were consistently allocated to a specific node.

Figure 13 displays the reflectivity-altitude joint histogram for each node in the CR. Examination of the joint histograms displays a clear ordering which is in line with previous discussion. In particular, the top left of the 5×3 SOM (node I1) is predominantly related to high-level clouds, while the bottom right of the SOM is related to low-level cloud. Node I1 appears to be associated with high-level cloud in the altitude range 12–14 km primarily, with some signs of potentially deeper cloud. Our earlier interpretation that node I1 represents stratiform anvil clouds associated with mesoscale convective systems and cirrus cloud appears to be supported by the CloudSat observations. Nodes I6 and I11 also appear to be related to cirrus. Nodes I2 to I5 are related to deep cloud with high cloud tops (of varying heights) likely related to the storm tracks. While node I8 is very obviously related to clear-sky conditions. Finally, nodes I14 and I15 are associated with low-level thin cloud and their geographic position (see Figure 3) further characterizes them as being associated with stratocumulus and stratus cloud decks. The inability of CloudSat to resolve cloud below 1 km due to ground clutter (Mace et al., 2009) likely means that the cloud fractions associated with these types are underestimated. In particular, the MODIS and ISCCP cloud covers linked to these nodes are significantly higher than the values derived from CloudSat. Overall, Figure 13 demonstrates that the current CR produces CloudSat composites which correspond well to the interpretations identified using the ISCCP observations. In fact, comparison of

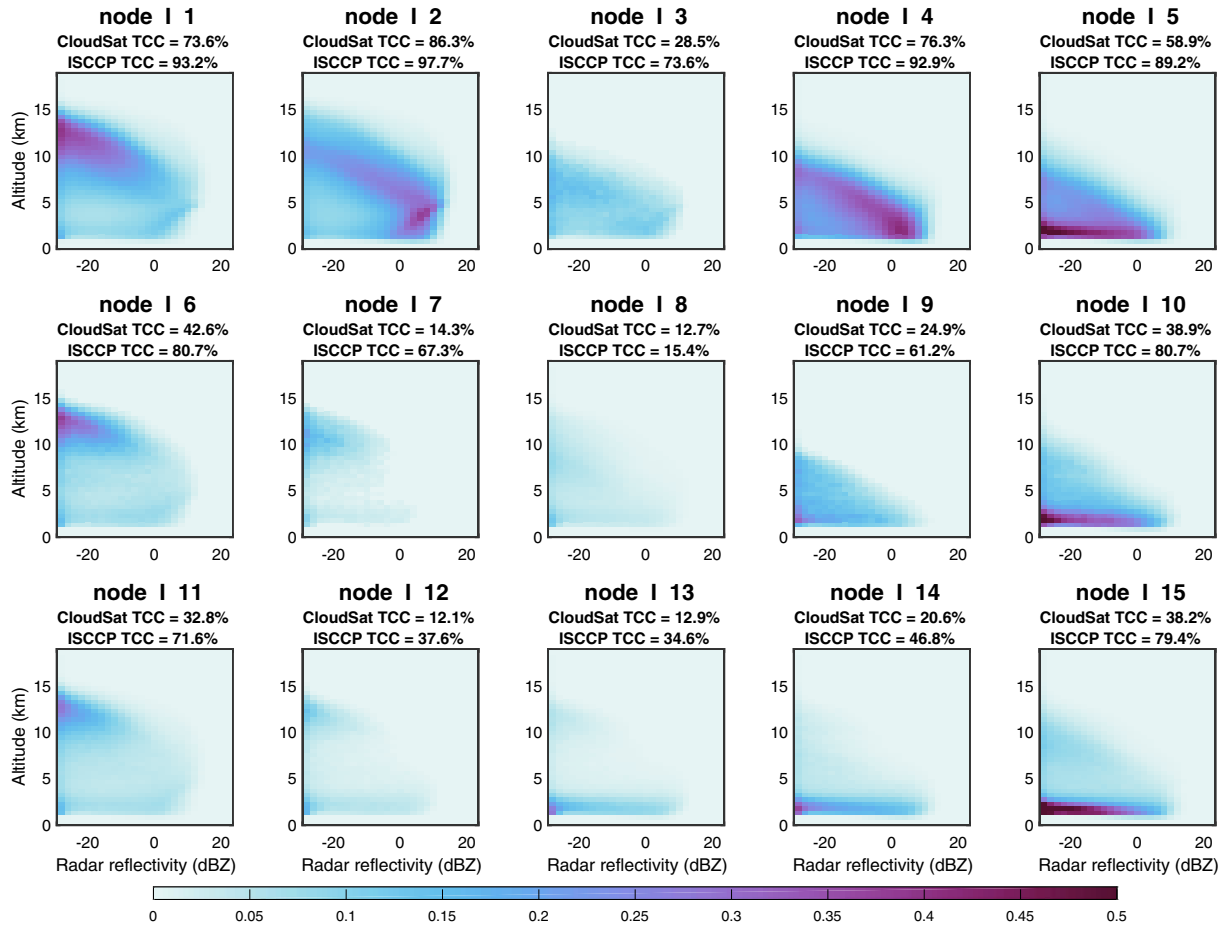

Figure 13. Global mean joint histograms of reflectivity by altitude for each of the International Satellite Cloud Climatology Project-derived cloud regimes. Each histogram is normalized such that the sum of the counts is proportional to the cloud fraction. The CloudSat-derived cloud fraction is also shown for each regime.

Figure 13 with Figure 3 in Leinonen et al. (2016) suggests that this classification may be less ambiguous than that previous study.

Figure 14 displays reflectivity-altitude joint histograms for each node in the DR. The CloudSat joint histograms for the various nodes show patterns that match with previous interpretation of Figure 8. In particular, the top left node (node $\omega 1$) is connected to high-level cloud and the bottom right node (node $\omega 12$) is related to low-level clouds. However, the various CloudSat joint histograms are more similar to each other than those in the CR classification (cf. Figures 13 and 14). There is also an absence of a clear-sky node and nodes connected to cirrus, thus this classification appears to produce a less distinct set of classes than those derived from the CR scheme. Correlation coefficients between the composite CloudSat joint histograms for different nodes can be used to derive statistics using the various permutations, these statistics being displayed in Table 1.

Table 1
Statistics of Correlation Coefficients Between the Composite CloudSat Joint Histograms for the Different Nodes in the Cloud and Dynamic Regimes

	Cloud regime	Dynamic regime
Minimum	−0.74	−0.56
Lower quartile	−0.17	0.25
Median	0.01	0.59
Upper	0.61	0.82
Maximum	0.97	0.96

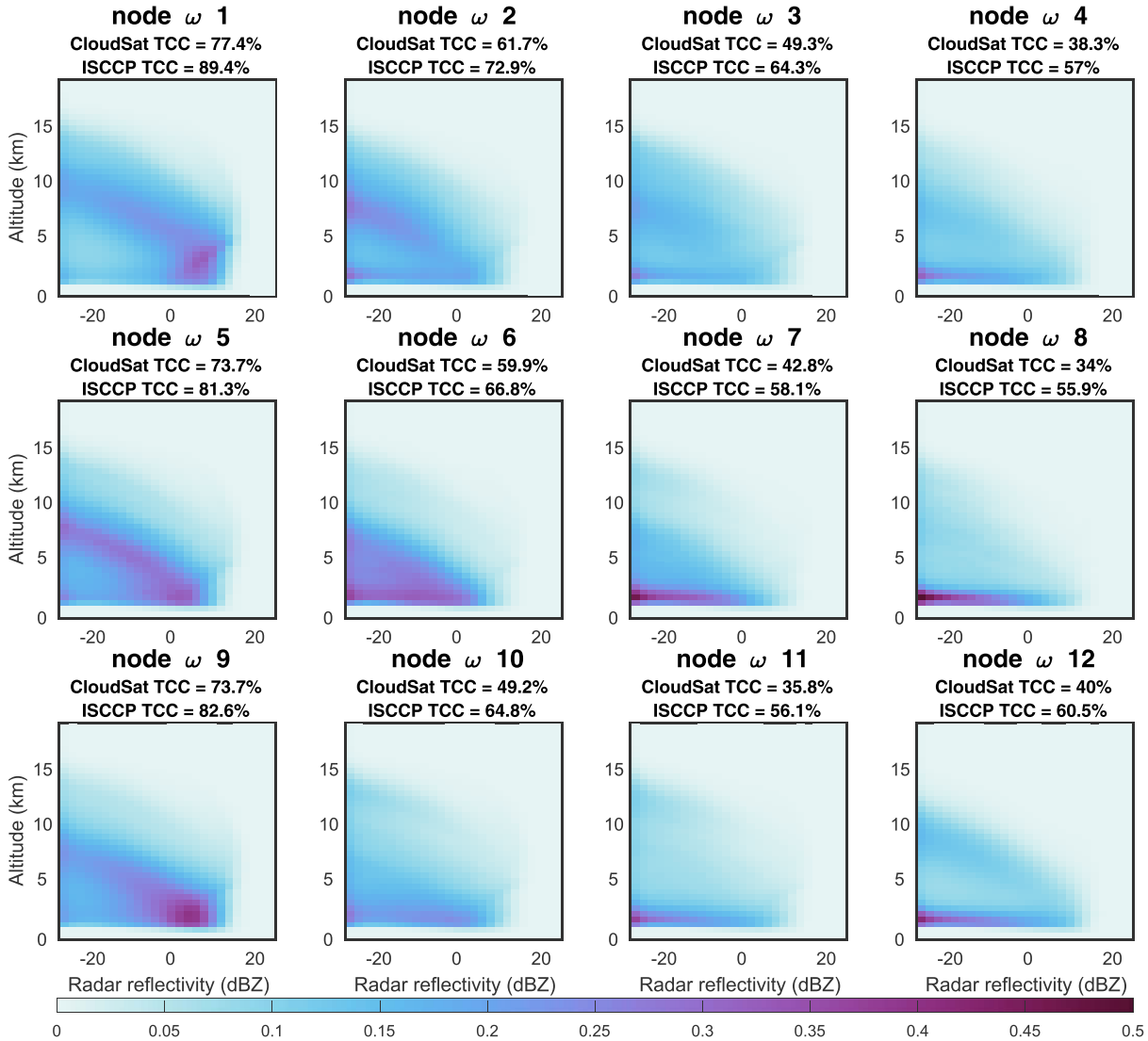

Figure 14. As in Figure 13 except for the dynamic regimes derived from ERA-Interim pressure vertical velocity data. TCC = total cloud cover; ISCCP = International Satellite Cloud Climatology Project.

Examination of the statistics in Table 1 shows that the median correlation between nodes in the CR (0.01) is very much smaller than that for the DR (0.59) which clearly identifies that the CR classification covers a wider range and more distinct set of cloud types than the DR scheme. The minimum and lower and upper quartiles also display the same pattern. However, the CloudSat composites with the maximum correlation is higher for the CR than the DR suggesting that two of the CloudSat joint histograms derived for the different CR nodes are very highly correlated. Inspection indicates that this correlation is linked to nodes I6 and I11, however the TCC derived from CloudSat is significantly larger in node I6 compared to I11 (42.6% to 32.8%, respectively), and thus these two nodes appear to be scaled versions of each other. Correlations between individual node's CloudSat joint histograms and the global average CloudSat joint histogram were also examined, the lower and upper quartiles of these correlations for the CR were 0.19 and 0.89, while those for the DR were 0.74 and 0.87. Thus, the range of these correlations is significantly greater for the CR than DR relative to the global mean pattern again suggesting that the CR representation characterizes a wider range of cloud types.

5. Discussion and Conclusions

In this study, we created a CR classification derived from ISCCP D1 observations using the SOM clustering technique and also produced a DR classification using the same clustering methodology applied to ERA-Interim

pressure vertical velocity profile output. Our results show that the CR created in this study is a refinement of that previously discussed in McDonald et al. (2016). In particular, we used the distribution of Pearson correlation coefficients between the representative CR node patterns and the data assigned to each node (see Figure 2) as an intracluster similarity metric and showed that the CR developed has higher intracluster similarity than the classification in McDonald et al. (2016). Analysis of that intracluster metric also suggests that the attribution of specific joint histograms using the 42 element vector Euclidean distance metric is preferable to the technique detailed in Williams and Webb (2009). An examination of the pressure vertical velocity profiles relationships to nodes in that CR (see Figure 4) also exhibits a clear ordering and clusters connected to high-level cloud are now more consistent with previous studies (Tan et al., 2013; Tselioudis et al., 2013). We have also demonstrated that the pressure vertical velocity at 500 hPa associated with each CR node displays clear ordering (see Figure 5) and that vertical velocity is an important driver of the observed cloud properties as we might expect. However, each CR node displays intracluster variability to varying degrees which supports the hypothesis in Leinonen et al. (2016) that variations in cloud properties within clusters are driven by meteorological variations. For example, the normalized vertical velocity anomalies at 500 hPa shown in Figure 5 display coherent patterns with the geographical variation in LW CRE for each node displayed in Figure 11.

Examination of independent data composited based on the CR classification also shows the quality of the current CR. In the spirit of work detailed in Leinonen et al. (2016), we examined the regional variation within nodes connected to the CR classification using normalized values of the LW CRE derived from ISCCP FD data. Examination of Figure 11 clearly shows regional variability is observed. However, the geographic variation in the normalized LW CRE is relatively small in most nodes for the CR scheme. We attribute the variability in the remaining nodes to latitudinal changes in the height of the tropopause. An interpretation driven by the predominantly latitudinal variability in the high cloud top states in the CR scheme in Figure 11. Composites of CloudSat data shown in Figure 13 demonstrate that the CR scheme produces representative reflectivity-altitude joint histograms which correspond well to the interpretations identified using the ISCCP observations alone further supporting the usefulness of this classification. One problem with the CR scheme is the potential for different satellites outputs to mean that CR classifications include instrumental artifacts, for example the discontinuity near the international date line in node 11 of the CR (see Figure 3), this is currently the subject of follow-up work.

The DR classification derived solely from ERA-Interim pressure vertical velocity output produces a set of RFO geographical maps (see Figure 7) which have similar features to those derived using the CR scheme (Figure 2). Figure 8 also displays composites of the ISCCP D1 joint histograms associated with the DR nodes (Figure 6) and shows a clear ordering with largest negative pressure vertical velocities (connected to ascent) being related to clouds with high tops (low pressure) and those linked to subsidence connected to clouds with low tops (high pressures) in the ISCCP composites. This displays the general utility of the DR scheme for cloud classification. However, analysis of the DR classification suggests weaknesses relative to the CR classification. In particular, our measure of intracluster similarity suggests that the DR methodology does not produce as coherent a classification as the CR scheme when examining correlations in the ISCCP D1 data set (see Figures 2a and 9a). This is despite analysis in Figure 9b which suggests that the DR classification is sound when we examine the representative pressure vertical velocity profiles against profiles assigned to a specific DR node.

Comparison of independent data sets also identifies the poorer performance of the DR scheme. In particular, Figures 11 and 12 shows that the geographic variation in the normalized LW CRE for specific DR nodes is very large compared to that for the CR scheme. This result implies that the DR scheme produces less distinct cloud groupings with a large spread of LW CRE when compared to the CR clusters. Analysis of the DR composite CloudSat reflectivity-altitude joint histograms (see Figure 14) also shows a narrower range of distinct cloud types, with no composites connected to clear skies or cirrus cloud. The CloudSat composites for the DR scheme are also considerably less independent than those from the CR scheme (see Table 1), highlighting that when the results of the two schemes are compared with independent cloud data, the CR classification outperforms the DR scheme.

The results in Figure 10 in McDonald et al. (2016) show that changes in LTS, ω, and the Total Column Water Vapor all potentially have a relationship with the cloud type observed, as might be expected based on previous studies. However, we choose to form our DR using only variations in the pressure vertical velocity. This decision was partly associated with the distinct differences in this variable identified in McDonald et al. (2016), but also because the use of a mixture of meteorological variables in a SOM framework would cause an inherent

assumption in our analysis. In particular, the use of multiple variables requires either normalization or weighting of the various meteorological parameters and ingrains an inherent assumption on the relative importance of various variables into our analysis. The results presented are therefore clearly not definitive as any classification can be enhanced. Further work will therefore attempt to develop a DR classification with a wider range of meteorological parameters to determine whether the DR classification can be improved. However, we would argue that these results represent a comparison between a CR and DR classification of similar complexity. In particular, given studies which have simply used the vertical velocity at 500 hPa, we would argue that our scheme is a useful starting point.

Analysis of the contingency table in Figure 10 shows little association between the CR and DR schemes. Though, nodes I1–I4 in the CR, displayed in Figure 1, have higher occurrences than the expected value for vertical velocity regimes connected to the left hand column of the SOM displayed in Figure 6 (ω1, ω5, and ω9). Thus, the nodes connected to ISCCP observations with high cloud tops are strongly connected to vertical velocity profiles with high ascent rates. A result that is supported by Figure 12, which suggests that the DR scheme performs better in regions of ascent. We interpret this as reflecting the fact that other factors such as the LTS and the availability of water vapor are likely more important in regions of subsidence.

Given the lack of association between the two schemes, further work could focus on the development of hybrid schemes and the analysis of data using both schemes. For example, Williams and Bodas-Salcedo (2017) argue that the best way to minimize issues around compensating model errors, observational error and model-observation comparison issues, is to routinely evaluate cloud in GCMs against a comprehensive set of different observational data sets, using satellite simulators where appropriate and using a range of diagnostic techniques. The fact that the DR and CR appear to have different strengths relative to cloud observations suggests that the use of multiple schemes adds value. In addition, the DR and CR analysis provides independent information which suggests that two stage classifications using cloud observations and meteorological data could be of high value. Gryspeerdt et al. (2017) have also advocated for the combination of dynamical and CRs and the utility of this approach.

The analysis presented in the current study suggests that the two schemes are largely independent and combinations of these classifications could add value to existing methodologies. However, if only one methodology is to be used to examine cloud properties then a CR approach is preferable based on internal consistency within the clusters when compared to the DR derived from the vertical velocity profile alone (c.f. Figures 2 and 8). Comparison with two independent data sets, ISCCP FD and CloudSat, also supports this conclusion for a DR scheme that includes only vertical velocities.

Acknowledgments
We would like to thank the numerous people that helped to create the ISCCP data set. The ISCCP D1 data used was obtained from the NASA Langley Research Center Atmospheric Science Data Center (http://eosweb.larc.nasa.gov). The ISCCP FD data were accessed via the ISCCP NASA Goddard Institute for Space Studies page (http://isccp.giss.nasa.gov). ERA-Interim data provided courtesy of ECMWF (http://apps.ecmwf.int). The CloudSat data used in this study were obtained from the CloudSat Data Processing Center (http://www.cloudsat.cira.(colostate.edu). This work was funded as part of two projects within the Deep South National Science Challenge.

References

Bony, S., Dufresne, J. L., Le Treut, H., Morcrette, J. J., & Senior, C. (2004). On dynamic and thermodynamic components of cloud changes. *Climate Dynamics*, *22*(2-3), 71–86. https://doi.org/10.1007/s00382-003-0369-6

Chen, Y. H., & Del Genio, A. D. (2009). Evaluation of tropical cloud regimes in observations and a general circulation model. *Climate Dynamics*, *32*(2-3), 355–369. https://doi.org/10.1007/s00382-008-0386-6

Coggins, J. H. J., McDonald, A. J., & Jolly, B. (2014). Synoptic climatology of the Ross Ice Shelf and Ross Sea region of Antarctica: K-means clustering and validation. *International Journal of Climatology*, *34*(7), 2330–2348. https://doi.org/10.1002/joc.3842

Dee, D. P., Uppala, S. M., Simmons, A. J., Berrisford, P., Poli, P., Kobayashi, S., et al. (2011). The ERA-Interim reanalysis: Configuration and performance of the data assimilation system. *Quarterly Journal of the Royal Meteorological society*, *137*(656), 553–597.

Feldstein, S. B., & Lee, S. (2014). Intraseasonal and interdecadal jet shifts in the Northern Hemisphere: The role of warm pool tropical convection and sea ice. *Journal of Climate*, *27*(17), 6497–6518. https://doi.org/10.1175/jcli-d-14-00057.1

Field, P. R., & Wood, R. (2007). Precipitation and cloud structure in midlatitude cyclones. *Journal of Climate*, *20*(2), 233–254. https://doi.org/10.1175/jcli3998.1

Gibson, P. B., Perkins-Kirkpatrick, S. E., Uotila, P., Pepler, A. S., & Alexander, L. V. (2017). On the use of self-organizing maps for studying climate extremes. *Journal of Geophysical Research: Atmospheres*, *122*, 3891–3903. https://doi.org/10.1002/2016jd026256

Gryspeerdt, E., Quaas, J., Goren, T., Klocke, D., & Brueck, M. (2017). Technical note: An automated cirrus classification. *Atmospheric Chemistry and Physics Discussions*, *2017*, 1–18. https://doi.org/10.5194/acp-2017-723

Gryspeerdt, E., Stier, P., & Partridge, D. G. (2014). Satellite observations of cloud regime development: The role of aerosol processes. *Atmospheric Chemistry and Physics*, *14*(3), 1141–1158. https://doi.org/10.5194/acp-14-1141-2014

Haynes, J. M., Jakob, C., Rossow, W. B., Tselioudis, G., & Brown, J. (2011). Major characteristics of Southern Ocean cloud regimes and their effects on the energy budget. *Journal of Climate*, *24*(19), 5061–5080. https://doi.org/10.1175/2011jcli4052.1

Haynes, J. M., Marchand, R. T., Luo, Z., Bodas-Salcedo, A., & Stephens, G. L. (2007). A multipurpose radar simulation package: QuickBeam. *Bulletin of the American Meteorological Society*, *88*(11), 1723–1727. https://doi.org/10.1175/bams-88-11-1723

Jakob, C. (2003). An improved strategy for the evaluation of cloud parameterizations in GCMS. *Bulletin of the American Meteorological Society*, *84*(10), 1387–1401. https://doi.org/10.1175/bams-84-10-1387

Jakob, C., & Tselioudis, G. (2003). Objective identification of cloud regimes in the tropical western Pacific. *Geophysical Research Letters*, *30*(21), 2082. https://doi.org/10.1029/2003GL018367

Jiang, J. H., Su, H., Zhai, C. X., Perun, V. S., Del Genio, A., Nazarenko, L. S., et al. (2012). Evaluation of cloud and water vapor simulations in CMIP5 climate models using NASA "A-Train" satellite observations. *Journal of Geophysical Research*, *117*, 24. https://doi.org/10.1029/2011jd017237

Jolly, B., Kuma, P., McDonald, A., & Parsons, S. (2017). Needs update : An analysis of the cloud environment over the Ross Sea and Ross Ice Shelf using CloudSat/CALIPSO satellite observations: The importance of synoptic forcing. *Atmospheric Chemistry and Physics Discussions*, *2017*, 1–27. https://doi.org/10.5194/acp-2017-547

Klein, S. A., & Hartmann, D. L. (1993). The seasonal cycle of low stratiform clouds. *Journal of Climate*, *6*(8), 1587–1606. https://doi.org/10.1175/1520-0442

Kohonen, T. (1990). The self-organizing map. *Proceedings of the IEEE*, *78*(9), 1464–1480. https://doi.org/10.1109/5.58325

Lau, N. C., & Crane, M. W. (1995). A satellite view of synoptic-scale organization of cloud properties in midlatitude and tropical circulation systems. *Monthly Weather Review*, *123*(7), 1984–2006. https://doi.org/10.1175/1520-0493

Leinonen, J., Lebsock, M. D., Oreopoulos, L., & Cho, N. (2016). Interregional differences in MODIS-derived cloud regimes. *Journal of Geophysical Research: Atmospheres*, *121*, 11,648–11,665. https://doi.org/10.1002/2016jd025193

Li, Y., Thompson, D. W. J., Stephens, G. L., & Bony, S. (2014). A global survey of the instantaneous linkages between cloud vertical structure and large-scale climate. *Journal of Geophysical Research: Atmospheres*, *119*, 3770–3792. https://doi.org/10.1002/2013jd020669

Mace, G. G., & Wrenn, F. J. (2013). Evaluation of the hydrometeor layers in the East and West Pacific within ISCCP cloud-top pressure-optical depth bins using merged CloudSat and CALIPSO data. *Journal of Climate*, *26*(23), 9429–9444. https://doi.org/10.1175/jcli-d-12-00207.1

Mace, G. G., Zhang, Q. Q., Vaughan, M., Marchand, R., Stephens, G., Trepte, C., & Winker, D. (2009). A description of hydrometeor layer occurrence statistics derived from the first year of merged CloudSat and CALIPSO data. *Journal of Geophysical Research*, *114*, 17. https://doi.org/10.1029/2007jd009755

Marchand, R., Ackerman, T., Smyth, M., & Rossow, W. B. (2010). A review of cloud top height and optical depth histograms from MISR, ISCCP, and MODIS. *Journal of Geophysical Research*, *115*, 25. https://doi.org/10.1029/2009jd013422

Marchand, R., Beagley, N., & Ackerman, T. P. (2009). Evaluation of hydrometeor occurrence profiles in the multiscale modeling framework climate model using atmospheric classification. *Journal of Climate*, *22*(17), 4557–4573. https://doi.org/10.1175/2009jcli2638.1

McDonald, A. J., Cassano, J. J., Jolly, B., Parsons, S., & Schuddeboom, A. (2016). An automated satellite cloud classification scheme using self-organizing maps: Alternative ISCCP weather states. *Journal of Geophysical Research: Atmospheres*, *121*, 13,009–13,030. https://doi.org/10.1002/2016JD025199

Medeiros, B., & Stevens, B. (2011). Revealing differences in GCM representations of low clouds. *Climate Dynamics*, *36*(1-2), 385–399. https://doi.org/10.1007/s00382-009-0694-5

Muhlbauer, A., McCoy, I. L., & Wood, R. (2014). Climatology of stratocumulus cloud morphologies: Microphysical properties and radiative effects. *Atmospheric Chemistry and Physics*, *14*(13), 6695–6716. https://doi.org/10.5194/acp-14-6695-2014

Nam, C. C. W., & Quaas, J. (2013). Geographically versus dynamically defined boundary layer cloud regimes and their use to evaluate general circulation model cloud parameterizations. *Geophysical Research Letters*, *40*, 4951–4956. https://doi.org/10.1002/grl.50945

Oreopoulos, L., Cho, N., & Lee, D. (2017). Using MODIS cloud regimes to sort diagnostic signals of aerosol-cloud-precipitation interactions. *Journal of Geophysical Research: Atmospheres*, *122*, 5416–5440. https://doi.org/10.1002/2016jd026120

Oreopoulos, L., Cho, N., Lee, D., & Kato, S. (2016). Radiative effects of global MODIS cloud regimes. *Journal of Geophysical Research: Atmospheres*, *121*, 2299–2317. https://doi.org/10.1002/2015jd024502

Oreopoulos, L., Cho, N., Lee, D., Kato, S., & Huffman, G. J. (2014). An examination of the nature of global MODIS cloud regimes. *Journal of Geophysical Research: Atmospheres*, *119*, 8362–8383. https://doi.org/10.1002/2013jd021409

Oreopoulos, L., & Rossow, W. B. (2011). The cloud radiative effects of International Satellite Cloud Climatology Project weather states. *Journal of Geophysical Research*, *116*, 22. https://doi.org/10.1029/2010jd015472

Press, W. H., Teukolsky, S. A., Vettering, W. T., & Flannery, B. P. (1992). *Numerical recipes in Fortran 77* (2nd ed.). Cambridge: Cambridge University Press.

Rossow, W. B., & Schiffer, R. A. (1991). ISCCP cloud data products. *Bulletin of the American Meteorological Society*, *72*(1), 2–20. https://doi.org/10.1175/1520-0477

Rossow, W. B., & Schiffer, R. A. (1999). Advances in understanding clouds from ISCCP. *Bulletin of the American Meteorological Society*, *80*(11), 2261–2287. https://doi.org/10.1175/1520-0477

Sammon, J. W. (1969). A nonlinear mapping for data structure analysis. *IEEE Transactions on Computers*, *C18*(5), 401–409. https://doi.org/10.1109/t-c.1969.222678

Schuddeboom, A., McDonald, A. J., Morgenstern, O., Harvey, M., & Parsons, S. (2018). Regional regime-based evaluation of present-day general circulation model cloud simulations using self-organizing maps. *Journal of Geophysical Research: Atmospheres*, *123*, 4259–4272. https://doi.org/10.1002/2017jd028196

Stephens, G. L., Vane, D. G., Tanelli, S., Im, E., Durden, S., Rokey, M., et al. (2008). CloudSat mission: Performance and early science after the first year of operation. *Journal of Geophysical Research*, *113*, 18. https://doi.org/10.1029/2008jd009982

Su, H., Jiang, J. H., Vane, D. G., & Stephens, G. L. (2008). Observed vertical structure of tropical oceanic clouds sorted in large-scale regimes. *Geophysical Research Letters*, *35*, 6. https://doi.org/10.1029/2008gl035888

Su, H., Jiang, J. H., Zhai, C. X., Perun, V. S., Shen, J. T., Del Genio, A., et al. (2013). Diagnosis of regime-dependent cloud simulation errors in CMIP5 models using "A-Train" satellite observations and reanalysis data. *Journal of Geophysical Research: Atmospheres*, *118*, 2762–2780. https://doi.org/10.1029/2012jd018575

Tan, J., Jakob, C., & Lane, T. P. (2013). On the identification of the large-scale properties of tropical convection using cloud regimes. *Journal of Climate*, *26*(17), 6618–6632. https://doi.org/10.1175/jcli-d-12-00624.1

Taylor, P. C., Kato, S., Xu, K. M., & Cai, M. (2015). Covariance between Arctic sea ice and clouds within atmospheric state regimes at the satellite footprint level. *Journal of Geophysical Research: Atmospheres*, *120*, 12,656–12,678. https://doi.org/10.1002/2015jd023520

Tselioudis, G., Rossow, W., Zhang, Y. C., & Konsta, D. (2013). Global weather states and their properties from passive and active satellite cloud retrievals. *Journal of Climate*, *26*(19), 7734–7746. https://doi.org/10.1175/jcli-d-13-00024.1

Williams, K. D., & Bodas-Salcedo, A. (2017). A multi-diagnostic approach to cloud evaluation. *Geoscientific Model Development Discussions*, *2017*, 1–44. https://doi.org/10.5194/gmd-2016-295

Williams, K. D., & Brooks, M. E. (2008). Initial tendencies of cloud regimes in the Met Office Unified Model. *Journal of Climate*, *21*(4), 833–840. https://doi.org/10.1175/2007jcli1900.1

Williams, K. D., & Webb, M. J. (2009). A quantitative performance assessment of cloud regimes in climate models. *Climate Dynamics*, *33*(1), 141–157. https://doi.org/10.1007/s00382-008-0443-1

Zhang, Y. Y., Klein, S., Mace, G. G., & Boyle, J. (2007). Cluster analysis of tropical clouds using CloudSat data. *Geophysical Research Letters*, *34*, 6. https://doi.org/10.1029/2007gl029336

Zhang, Y. C., Rossow, W. B., Lacis, A. A., Oinas, V., & Mishchenko, M. I. (2004). Calculation of radiative fluxes from the surface to top of atmosphere based on ISCCP and other global data sets: Refinements of the radiative transfer model and the input data. *Journal of Geophysical Research*, *109*, 27. https://doi.org/10.1029/2003jd004457